Physics-based models of ground deformation and extrusion rate at effusively erupting volcanoes

Kyle Anderson[1] and Paul Segall[1]

Received 8 September 2010; revised 14 April 2011; accepted 19 April 2011; published 16 July 2011.

[1] We present a model of effusive silicic volcanic eruptions which relates magma chamber and conduit physics to time-dependent data sets, including ground deformation and extrusion rate. The model involves a deflating chamber which supplies Newtonian magma through a cylindrical conduit. Solidification is approximated as occurring at fixed depth, producing a solid plug that slips along its margins with rate-dependent friction. Changes in tractions acting on the chamber and conduit walls are used to compute surface deformations. Given appropriate material properties and initial conditions, the model predicts the full evolution of an eruption, allowing us to examine the dependence of observables on initial chamber volume, overpressure, and volatile content. Employing multiple data sets in combination with a physics-based model allows for better constraints on these parameters than is possible using kinematic idealizations. Modeling posteruptive deformation provides an improved constraint on the rate of influx into the magma chamber from deeper sources. We compare numerical results to analytical approximations and to data from the 2004–2008 eruption of Mount St. Helens. For nominal parameters the balance between magma chamber pressure and frictional resistance of the solid plug controls the evolution of the eruption, with little contribution from the fluid magma below the idealized crystallization depth. While rate-dependent plug friction influences the time-dependent evolution of the eruption, it has no control on the final chamber pressure or extruded volume.

Citation: Anderson, K., and P. Segall (2011), Physics-based models of ground deformation and extrusion rate at effusively erupting volcanoes, *J. Geophys. Res.*, *116*, B07204, doi:10.1029/2010JB007939.

1. Introduction

[2] Data collected at volcanoes, whether from InSAR, GPS, tilt, gravity, COSPEC, or other instruments or techniques, is most useful when interpreted in terms of physical models. Most models of volcano deformation are kinematic (they do not consider the physical and chemical processes that lead to changes in pressures acting on magma chamber walls) and are limited to idealized shapes such as spheres or ellipsoids in elastic half-spaces [e.g., *Mogi*, 1958; *Yang et al.*, 1988]. Because they are kinematic, they have no predictive capability and cannot be used to model the evolution of deformation with time given a set of initial conditions such as magma chamber overpressure and volume, and they are also poorly suited for predicting other types of data such as effusion rate or gravity change. Inversions for deformation data therefore typically consider only net deformations over some time period, ignoring the rich information contained in the details of the time series as well as valuable constraints that could be provided by additional data sets.

[3] Physics-based models of magma ascent and eruption are available, but typically do not consider interactions of the magma with the surrounding host rock and therefore cannot be used to predict ground deformation. Because these models are often strongly nonlinear, and behavior depends on parameter values and constitutive laws which are only poorly known, additional constraint by data is vitally important, but is not available because these models do not consider interaction with the host rock.

[4] In this work we develop a physics-based model of an effusive silicic eruption which links magmatic processes directly with observed ground deformation and effusion rate. The model is designed to replicate behavior commonly observed during effusive eruptions, in which extrusion rates (and ground deformation rates, if recorded) decline smoothly with time (Figure 1). The model is further specialized herein for a silicic, dome-building eruption of the type observed at Mount St. Helens (2004–2008); with modification, however, it could also be applied to other types of effusively erupting volcanoes. This approach has the potential to significantly improve constraints on magmatic processes while simultaneously enhancing our ability to understand and model a variety of geophysical time series.

[5] A following study (K. Anderson and P. Segall, Bayesian inversion of data from effusive volcanic eruptions using physics-based models: Application to Mount St. Helens 2004–2008, manuscript in preparation, 2011, hereafter referred

[1]Department of Geophysics, Stanford University, Stanford, California, USA.

0148-0227/11/2010JB007939

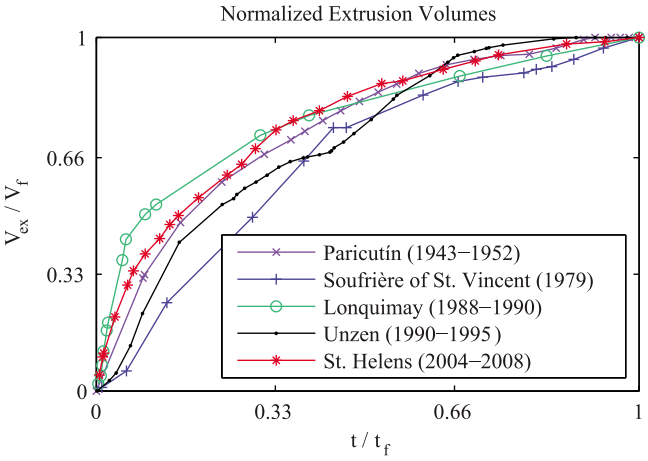

Figure 1. Lava extrusion time series at five volcanoes, normalized in time and volume. Paricutín and Lonquimay data are for tephra plus lava DRE (dense rock equivalent) and are taken from *Stasiuk et al.* [1993]; Soufriere of St. Vincent data are from *Huppert et al.* [1982]; Unzen data are from *Nakada et al.* [1999]; and Mount St. Helens data are from *Schilling et al.* [2008, also personal communication, 2010]. Durations of extrusion ranged from <6 months for Soufriere of St. Vincent to almost 10 years for Paricutin. Paricutin produced more than one billion m^3 of lava, while Soufriere of St. Vincent produced ~50 million m^3.

to as "part 2") will examine the use of this forward model to estimate eruptive parameters at Mount St. Helens using GPS and effusion rate data employing a Bayesian approach which allows us to evaluate full posterior probability distributions, rather than simply inverting for a single set of model parameters which "best" fits the data.

2. Previous Studies

[6] Models of magma flow through a conduit are used to explain observed phenomena including eruptive periodicity and the transition between effusive and explosive behavior [e.g., *Woods and Koyaguchi*, 1994; *Jaupart*, 1996; *Slezin*, 2003]. In simple form, these models consist of the laminar 1D steady state ascent of magma through a rigid cylinder [e.g., *Jaupart*, 1996; *Melnik and Sparks*, 1999, 2002; *Mastin and Ghiorso*, 2000]. Even these simple models may display strongly nonlinear behavior and have multiple steady state solutions due to nonlinearity in constitutive laws and dependencies between different parameters, and additional complexity is introduced by consideration of lateral variation of magma properties in the conduit [*Massol et al.*, 2001; *Collier and Neuberg*, 2006; *Mastin*, 2005], non-Newtonian rheologies [*Melnik and Sparks*, 2005], noncylindrical or depth-varying conduit geometries [*Costa et al.*, 2007a, 2007b; *de' Michieli Vitturia et al.*, 2008], and elastic or viscoelastic behavior of the conduit walls and/or inclusion of the magma chamber feeding the eruption [*Maeda*, 2000; *Barmin et al.*, 2002; *Costa et al.*, 2007a].

[7] Consideration of time-dependent behavior adds further complexity. Such behavior may occur over many different timescales due to changes in conduit size, nonlinear behavior associated with gas exsolution and crystal growth, or a time-varying magma chamber pressure [*Ramos*, 1995; *Barmin et al.*, 2003; *Proussevitch and Sahagian*, 2005; *Starostin et al.*, 2005; *Melnik and Sparks*, 2005, 2006; *Mason et al.*, 2006]. Time-dependent models with complex interactions may provide insight into the short-to intermediate-period oscillatory behavior often observed during eruptions. In contrast, quasi-exponential declines in extrusion rate often observed over long time periods may be explained with simple models of a deflating magma chamber coupled to Newtonian conduit flow [*Wadge*, 1981; *Stasiuk et al.*, 1993; *Segall et al.*, 2001; *Huppert and Woods*, 2002; *Woods and Huppert*, 2003] sometimes including rate-dependent slip of a solid plug in the upper conduit [*Mastin et al.*, 2008].

[8] Complex models with numerous material parameters require constraint from laboratory or field observations, yet few conduit models consider how magma or magma/rock interactions generate observable geophysical signals, and they remain unconstrained by data except time-dependent extrusion rate. Exceptions include *Nishimura* [2006, 2009], who model time-dependent ground deformation due to magma ascent and degassing in an open conduit, *Lensky et al.* [2008] for tilt due to cycles of plug slip and degassing, and *Hautmann et al.* [2009], who compute ground deformation due to a dike/conduit system with the geometry used by *Costa et al.* [2007a, 2007b] and the pressure changes calculated therein. Finally, *Mastin et al.* [2008, 2009] use time-dependent models of the effusive eruption of Mount St. Helens (2004–2008) along with deformation and extrusion rate data to constrain aspects of the midcrustal magma chamber that fed that eruption.

3. Model Design

[9] Oscillatory and chaotic behavior is often observed at erupting volcanoes, but over long periods of time many volcanoes display a gradual reduction in effusion rate suggestive of the deflation of a pressurized magma chamber (Figure 1). Our goal in this work is to relate well-established conduit and magma chamber physics to geophysical observables, and we seek a balance between simplicity and solution speed on the one hand, and model complexity and realism on the other. Here we do not seek to model oscillatory eruptive behavior, and we disregard certain processes such as the kinetics of crystallization in order to focus on general features of the magmatic system (chamber volume, influx rate, etc.) with a relatively simple forward model that may be run tens of thousands of times in order to perform Monte Carlo inversions. Inspiration for this analysis comes from the 2004–2008 eruption of Mount St. Helens, and while the resulting model cannot be considered general for all effusive eruptions, with appropriate modification our approach should be generally applicable to many volcanoes displaying a gradual decline in eruptive activity.

[10] We assume a model geometry consisting of an ellipsoidal magma chamber coupled to the surface by a thin, vertical, cylindrical conduit (Figure 2). Excess pressure in the magma chamber drives Newtonian flow of magma (containing melt, phenocryst, bubble, and dissolved gas phases) through the conduit. At the top of the conduit the magma solidifies into a solid plug which slips on cylindrical faults with rate-dependent friction. The physical model can

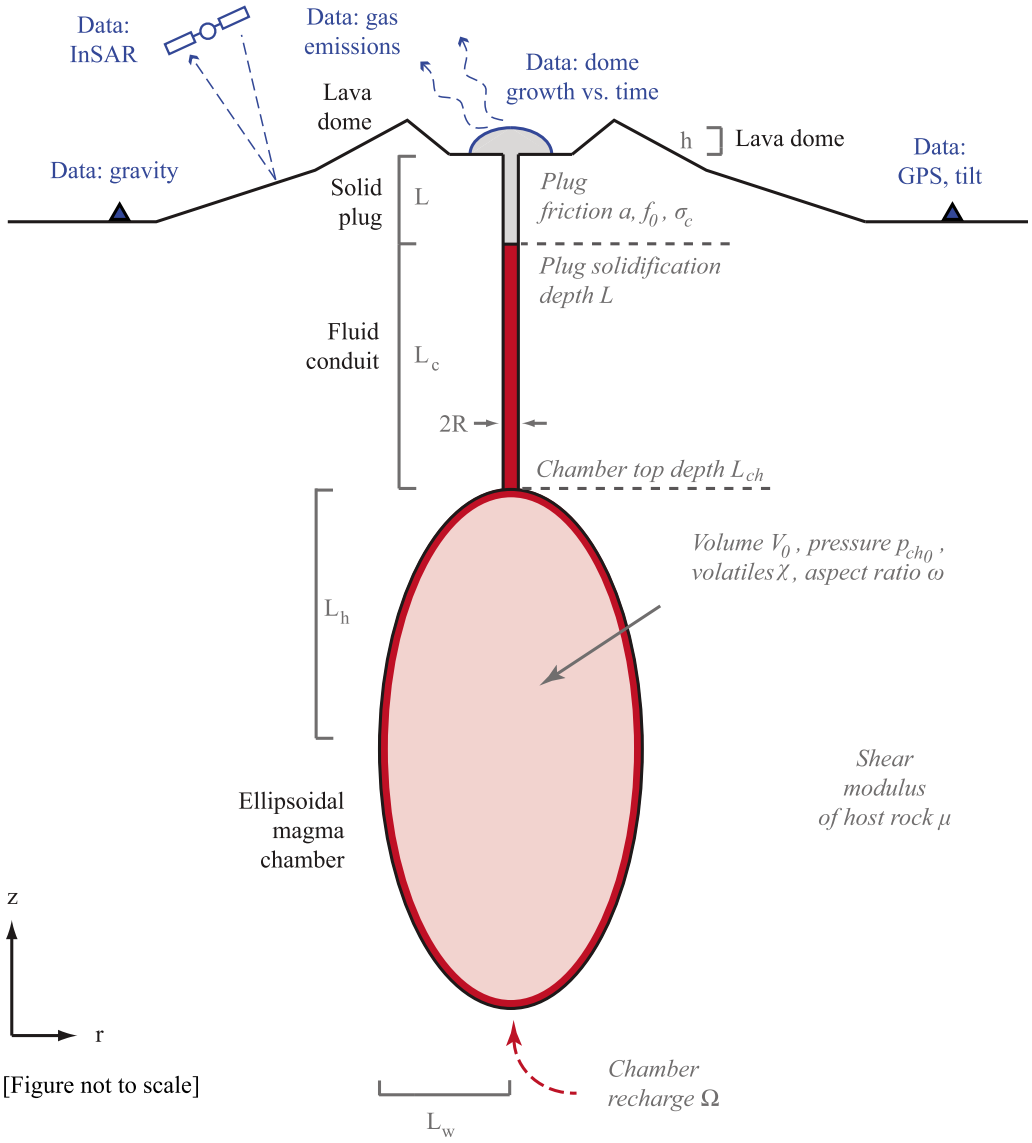

Figure 2. Model geometry and parameterization. An ellipsoidal magma chamber is connected to the surface by a thin, vertical, cylindrical conduit. The lower portion of the conduit contains magma, while the top portion is filled with a solid plug which slips along the conduit walls. Some key model parameters are shown in italics; these parameters may either be estimated in an inversion or taken from other sources (such as petrologic studies). Note that the surface may include topography of arbitrary complexity if Green's functions are estimated using numerical techniques. The model may be compared to a variety of data sets including deformation, time-dependent dome growth, and gas emissions.

be used to predict observables including ground deformation and extrusion rate (the focus of this study), as well as gas emissions, changes in gravity, and potentially seismicity (to be considered in future work). Pressure changes in the magma chamber and fluid conduit, and tractions along the length of the conduit, are used to calculate surface displacements in the surrounding elastic medium. Computing elastic Green's functions using numerical methods allows for the inclusion of topography and variations in material properties (layering, etc.) of arbitrary complexity in the predicted surface deformation.

[11] Model parameters are listed in Table 1 along with representative values.

3.1. Conduit

[12] Key physical processes occur in the conduit which play a critical role in controlling the evolution of an eruption and the transition between effusive and explosive behavior [e.g., *Jaupart*, 1996]. As magma ascends, pressure decreases and volatiles exsolve from the melt to form a bubble phase. The growth of bubbles leads to a reduction in bulk density and an increase in vertical velocity, and the reduction of dissolved volatiles increases melt viscosity. At low pressures, gas escape [*Diller et al.*, 2006] and decompression-driven crystallization [*Cashman and Blundy*, 2000] can result in the formation of semisolid plugs of rock in the upper conduit. Such plugs may play important roles in governing eruptive behavior: for example, extrusion rate

Table 1. Symbols and their nominal values[a]

Symbol	Description	Nominal Value or Equation
	Independent Variables	
z	Vertical spatial coordinate	-
r	Radial spatial coordinate	-
t	Time	-
	Unknowns in Numerical Solution	
$p(z, t)$	Pressure in conduit	-
$v(z, t)$	Magma velocity in conduit	-
$\rho(z, t)$	Bulk magma density in conduit	-
$p_{ch}(t)$	Pressure at top of magma chamber	-
	Geometry and Host Rock Parameterization	
R	Conduit radius	50 m
L	Length of solid plug	700 m
L_c	Length of fluid (Newtonian) conduit	4300 m
$h(t)$	Height of lava dome	0 m
ρ_p	Density of solid plug	2400 kg/m^3
μ, ν	Shear modulus and Poisson's ratio	20 GPa, 0.25
ω	Chamber aspect ratio (height/width)	5
V_0	Initial chamber volume	10 km^3
	Other Model Parameters (*Partial List*)	
p_{ch_0}	Initial pressure at top of magma chamber	130 MPa
χ_d^w, χ_T^c	Mass concentrations dissolved water, total CO_2	4.4 wt%, 2000 ppm
ϕ_{ch}	Mass fraction phenocrysts in chamber	45%
T	Temperature of melt	1123 K (850°C)
Ω	Chamber influx coefficient	0 m^3 day^{-1} MPa^{-1}
f_0	Friction: Nominal coefficient of friction	0.4
a, b	Friction: Direct and evolution effects	0.08 and 0
v_r	Friction: Reference velocity	0.001 m/s
σ_c	Friction: Effective normal stress coefficient	0.3
ρ_l	Density of host rock	2700 kg/m^3
ρ_λ^0	Nominal melt density	2200 kg/m^3
ρ_ϕ^0	Nominal phenocryst density	2600 kg/m^3
ρ_c^0	Nominal dissolved volatile density	741 kg/m^3
β_λ	Compressibility of melt	2×10^{-10} Pa^{-1}
β_ϕ	Compressibility of phenocrysts	2×10^{-11} Pa^{-1}
β_c	Compressibility of dissolved volatiles	1.38×10^{-10} Pa^{-1}
	Dependent Variables	
$p_{cc}(t)$	Pressure at center of magma chamber	-
$\chi_e^w(z, t)$, $\chi_e^c(z, t)$	Mass concentrations exsolved H_2O, CO_2	equations (4) and (5)
$\alpha(z, t)$	Bubble (exsolved volatile) mass fraction	-
$c(z, t)$	Dissolved volatile mass fraction	-
$\phi(z, t)$	Phenocryst mass fraction	-
$\lambda(z, t)$	Melt mass fraction	-
$S^w(z, t)$, $S^c(z, t)$	Volatile solubility in melt for H_2O, CO_2	*Liu et al.* [2005]
$\rho^*(z, t)$	Bulk magma density	equation (3)
$\rho_\alpha(z, t)$	Density of exsolved gas	equation (6)
$\rho_\lambda(z, t)$	Density of melt phase	equation (7)
$\rho_\phi(z, t)$	Density of phenocryst phase	equation (7)
$\rho_c(z, t)$	Density of dissolved volatile phase	equation (7)
$\eta(z, t)$	Effective magma viscosity	equation (8)
$\eta_\chi(z, t)$	Viscosity of crystal-free magma	*Hess and Dingwell* [1996]
$\eta_\phi(z, t)$	Viscosity increase due to phenocrysts	*Costa* [2005, see also arXiv:physics/0512173v2]
$\tau_p(t)$	Shear tractions on conduit walls due to plug	equations (10) and (11)
$\tau(z, t)$	Shear tractions on walls of fluid conduit	equation (25)
$\overline{\sigma}$	Average effective normal stress on plug	equation (12)
$\phi^v(z, t)$	Volume fraction phenocrysts	equation (A3)
$q_{in}(t)$	Volumetric flowrate into chamber (recharge)	equation (14)
$\beta_m(t)$	Compressibility of melt in chamber	equation (15a)
$\beta_{ch}(t)$	Compressibility of chamber	equation (15b)
$u(\mathbf{x}, t)$	Surface ground displacements	equation (26)
	Fixed Constants	
g	Gravity	9.81 m/s^2
R^w, R^c	Individual gas constants for H_20 and $C0_2$	461.5 and 188.9 J kg^{-1} K^{-1}

[a]Parentheses indicate functional relationships for spatial coordinate z and/or time t only; other relationships are not specified.

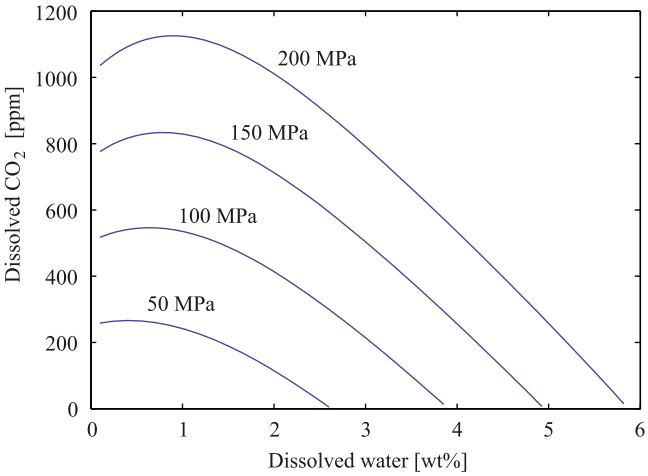

Figure 3. Isobaric solubility plot using the expressions of *Liu et al.* [2005] at 850°C. Each line represents the locus of all possible dissolved volatile concentrations for a melt in equilibrium with a CO_2 - H_2O fluid at the indicated pressure.

data often show a nonexponential decay with time [e.g., *Stasiuk et al.*, 1993; *Wadge*, 1981], which may be due in part to frictional sliding of a solid plug at shallow depth [*Mastin et al.*, 2008].

3.1.1. Conservation Laws

[13] Magma ascending from the chamber to the base of the solid plug is modeled as a compressible, multiphase Newtonian fluid. All phases are assumed to travel together at velocity $v(z, t)$ and at pressure $p(z, t)$ (see section 3.1.3 for a discussion of gas loss assumptions). Magma properties are averaged horizontally such that equations are one-dimensional along the vertical z axis. For laminar flow in a long thin cylindrical pipe with z positive upwards, momentum conservation is given by (section A1)

$$0 = \frac{\partial p}{\partial z} + \rho g + \frac{8\eta v}{R^2}, \tag{1}$$

where $\rho = \rho(z, t)$ is the depth- and time-dependent bulk magma density in the conduit, $\eta = \eta(z, t)$ is the bulk magma viscosity, and R is the conduit radius.

[14] For a cylindrical conduit, changes in radius due to reasonable pressure changes must be very small. Calculating radial displacements u_r on the walls of the cylinder assuming plane strain deformation, $u_r = \Delta pR/2\mu$ [*Timoshenko and Goodier*, 1970]. Assuming a pressure change of Δp = 20 MPa, conduit radius R = 50 m, and shear modulus μ = 20 GPa, radial displacements are 2.5 cm (less than 0.1% of the radius). Assuming therefore a constant radius R, as well as no gas loss, mass conservation in the conduit is given by

$$\frac{\partial \rho}{\partial t} = -\frac{\partial}{\partial z}(\rho v). \tag{2}$$

[15] The time-dependent term in equation (2) may be neglected only when magma ascent times are significantly shorter than the times associated with changes in eruption dynamics [*Ramos*, 1995; *Melnik and Sparks*, 2006]. Changes in eruption dynamics can be slow for effusive dome-building eruptions, but magma ascent rates are low and residence times are thus long. Rather than making a quasi steady state assumption, we use the transient expression above; the model therefore remains general and can be used to evaluate the importance of the time-dependent terms for different eruptions.

3.1.2. Magma

[16] We model a multiphase magma containing melt, phenocrysts, dissolved volatiles, and exsolved volatiles (bubbles), with mass fractions λ, ϕ, c, and α, respectively. Phenocrysts are carried upwards from the magma chamber without growth, and microlite crystallization occurs as a step function at a fixed solidification depth (section 3.1.4). Bulk density (section A3)

$$\rho^* = \left[\frac{1-\phi}{1+\chi_e+\chi_d}\left(\frac{\chi_e}{\rho_\alpha}+\frac{\chi_d}{\rho_c}+\frac{1}{\rho_\lambda}\right)+\frac{\phi}{\rho_\phi}\right]^{-1} \tag{3}$$

is an explicit function of pressure through the mass fractions and concentrations (section A2) of the different phases. Mass concentrations of total dissolved and exsolved volatiles, respectively, are given by χ_d and χ_e, and ρ_α, ρ_c, ρ_λ, and ρ_ϕ are the phase densities of the exsolved volatile, dissolved volatile, melt, and phenocryst phases, respectively.

[17] While many models utilize only a single volatile phase (H_2O) in the melt, *Mastin et al.* [2008] used the two-phase solubility code VolatileCalc [*Newman and Lowenstern*, 2002] and demonstrated the importance of considering both H_2O and CO_2, as gas exsolves more gradually over a wider range of pressures in the two-phase model and a sudden increase in compressibility at the water saturation pressure is thus avoided.

[18] We model combined H_2O and CO_2 solubility using relations S of *Liu et al.* [2005] (isobaric relationships are shown in Figure 3):

$$\chi_d^w = \chi_T^w - \chi_e^w = S^w(m^w, m^c, p, T), \tag{4}$$

$$\chi_d^c = \chi_T^c - \chi_e^c = S^c(m^w, m^c, p, T), \tag{5}$$

where T is the temperature of the melt, and assuming closed system degassing and neglecting crystallization, the total mass concentration of volatiles χ_T must remain constant and equal to the sum of dissolved and exsolved gases. Mole fractions m^w and m^c of water and carbon dioxide, respectively, are related by $m^w + m^c = 1$, and molar and mass concentrations are related by $\chi_e^w = \chi_e^c B m^w/m^c$, where B = 18.02/44.01 ≈ 0.41 is the ratio of the molecular mass of water to carbon dioxide.

[19] Given dissolved water χ_d^w (which may be estimated from petrologic analysis) and total carbon dioxide χ_T^c (which may be estimated by comparing CO_2 emissions and extruded dome volume [e.g., *Gerlach et al.*, 2008]) at p_{ch_0} at the top of the magma chamber at t = 0, we solve the resulting system of six equations for the six unknowns χ_T^w, χ_e^w, χ_d^c, χ_e^c, m^w, and m^c. With χ_T^w and χ_T^c (both of which remain constant) it is then possible to solve for dissolved and exsolved volatile mass fractions at any pressure (Figure 4).

[20] Partial pressures of H_2O and CO_2 in bubbles are calculated using $p^w = m^w p$ and $p^c = m^c p$, respectively. Using the ideal gas law [e.g., *Jaupart and Tait*, 1990], exsolved gas density ρ_α may be calculated using

$$\rho_\alpha = \frac{p^w}{R^w T} + \frac{p^c}{R^c T}, \tag{6}$$

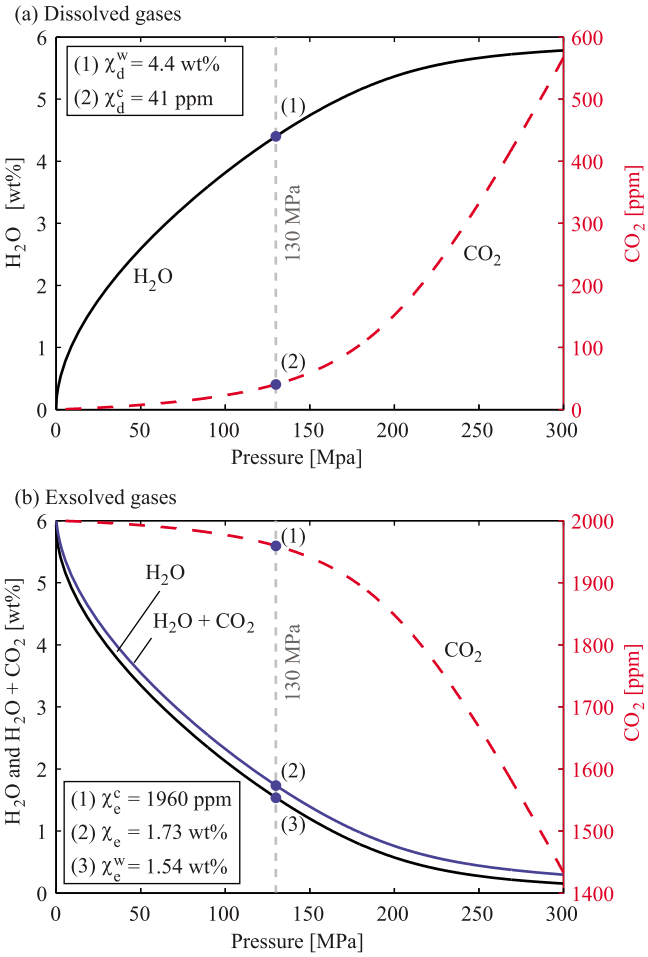

Figure 4. (a) Dissolved and (b) exsolved volatiles as functions of pressure assuming closed system degassing using *Liu et al.* [2005]. In this example, water χ_d^w = 4.4 wt% and total carbon dioxide χ_T^c = 2000 ppm are specified at 130 MPa (vertical dashed line). At 130 MPa, the melt contains 40 ppm dissolved CO_2 along with the 4.4 wt% water, while total exsolved gas concentration is 1.7 wt%. Note that deeper in a chamber (p > 200 MPa) the dissolved water concentration would exceed 5 wt%.

where R^w and R^c are the gas constants for water vapor and carbon dioxide.

[21] Assuming a linearized equation of state, phase densities of melt, phenocrysts, and dissolved volatiles may be calculated as functions of pressure with compressibilities β_λ, β_ϕ, and β_c, respectively, using [e.g., *Costa et al.*, 2009]

$$\rho_i = \rho_i^0(1 + \beta_i \Delta p), \qquad \text{for} \quad i = \lambda, \phi, c \tag{7}$$

where the ^{0} superscript indicates the nominal density at the reference pressure p^0, and $\Delta p = p - p^0$.

[22] Compressibilities of melt and phenocryst phases are taken from *Mastin et al.* [2008]. For dissolved volatiles we assume that density is controlled by the dominant water phase (neglecting CO_2), and use results of *Ochs and Lange* [1999], who report a nominal partial molar volume for water of $\overline{V}_{H_2O}$ = 2.29 × 10^{-5} m^3/mole (787 kg/m^3) at 1000°C and 0.1 MPa, independent of water concentration in the melt. At T = 850°C this yields a nominal density ρ_c^0 = 741 kg/m^3 using the thermal expansivity reported in the same study. Finally, we use a compressibility of β_c = 1.38 × 10^{-10} Pa^{-1} also from *Ochs and Lange* [1999]. Dissolved water is thus relatively compressible in the melt, although still highly incompressible compared to the gas phase which dominates system compressibility (see Table 1); however, we include compressibility of other phases for completeness.

[23] The viscosity η of a silicate melt is a complex function of melt composition, dissolved water content, temperature, phenocryst content, bubble content, and other effects. We estimate viscosity using the empirical results of *Hess and Dingwell* [1996] for viscosity η_χ of a crystal-free melt as a function of the mass concentration of dissolved water χ_d^w and temperature T, increased by a factor η_ϕ due to phenocryst content ϕ^v after *Costa* [2005, see also Comments on "viscosity of high crystal content melts: dependence on solid fraction," arXiv:physics/0512173v2] but neglect the effect of bubbles [*Llewellin and Manga*, 2005], such that

$$\eta = \eta_\chi(\chi_d^w, T)\eta_\phi(\phi^v), \tag{8}$$

where detailed expressions are given in the cited references.

3.1.3. Gas Loss

[24] Bubbles do not move easily through viscous silicic melts [e.g., *Eichelberger*, 1995] and bubble (or possibly fracture) connectivity and subsequent permeable gas flow is probably required for gas to escape from the conduit (either vertically or laterally). Several factors enhance degassing at shallow depths and restrict it at deeper depths, including much higher porosities in the shallow conduit and reduced wallrock permeability at depth. Because the conduit is capped by a solid plug and modeled as a fluid magma only at deep to intermediate depths, this suggests that gas loss from the conduit may not be significant in the context of the current model. This inference is supported by a 2D model of gas loss developed by *Collombet* [2009] for a 4.5 wt% melt which shows that conduit outgassing primarily influences the shallowest 500 m of the conduit. For simplicity, we therefore neglect conduit outgassing in this study; this assumption may somewhat bias velocities and densities in the upper conduit, but we postpone a more detailed analysis for future work.

3.1.4. Plug Formation

[25] Low ascent rates allow for extensive decompression crystallization in the shallow conduit and the formation of solid or semisolid plugs of rock [*Cashman et al.*, 2008]; extrusion of these plugs onto the surface in the form of spines has been observed at many eruptions including Mount St. Helens (2004–2008), Unzen (1991–1995), and Soufriere Hills (1995–present). Spine formation is favored at ascent rates of less than 1–5 × 10^{-4} m/s, such that magma ascent is slow relative to the kinetics of crystallization and dynamics of gas loss [*Cashman et al.*, 2008]. Higher ascent rates favor shear lobes, oscillatory or chaotic behavior, or even vulcanian explosions.

[26] In this work we focus on eruptions with low ascent rates and assume that decompression and volatile exsolution-driven crystallization processes are not limited by time but by pressure, and that the depth of crystallization remains constant despite changes in conduit pressure over the course of an eruption. We make use of petrologic observations to

directly enforce a fixed crystallization depth at the base of the solid plug. More realistically, a declining conduit pressure might result in a crystallization depth which increases with time, lengthening the solid plug over the course of the eruption and thereby increasing the total resistive force provided by the plug (see section 3.1.5). This, in turn, would likely hasten the end of the eruption, so our assumption of a constant crystallization depth probably biases our results toward extruded volumes and geodetic displacements which are too high.

[27] Because melt viscosity is highly nonlinear around the point at which crystals begin to strongly interact with one another [*Costa*, 2005], after *Barmin et al.* [2002] we assume a step transition between Newtonian fluid flow in the lower conduit and frictional slip of the solid plug in the upper conduit (but as noted we enforce this depth, rather than compute it as in the work of *Barmin et al.* [2002]).

[28] As material is extruded onto the surface, a dome may grow to height h with time (affecting vent pressure), or for simplicity it may be assumed that the rate of surface erosion equals the rate of extrusion such that h is constant. System response to sudden unloading caused by dome collapse is not examined in this study.

3.1.5. Motion of the Solid Plug

[29] The solid plug is subjected to an upwards force due to magma pressure in the conduit, and downward forces due to the weight of the plug and frictional resistance due to slip on the marginal faults (we neglect atmospheric pressure). Assuming that changes in extrusion rate are slow over the course of the eruption, such that inertia may be neglected, forces on the plug must balance [e.g., *Mastin et al.*, 2008]:

$$0 = p_p R - \rho_p R(L+h)g - 2L\tau_p, \tag{9}$$

where p_p is pressure at the base of the plug, ρ_p is the density of the plug, L is the length of the solid plug (distance from the surface to the depth of crystallization, not including dome height h), and τ_p is the velocity-dependent shear stress on the margins of the plug. Solving for τ_p yields

$$\tau_p = R\left[p_p - \rho_p(L+h)g\right]/2L, \qquad \text{for} \quad z > -L. \tag{10}$$

[30] The plug slips upwards along a cylindrical fault with rate-dependent friction. The choice of friction law is based on laboratory tests which indicate that the coefficient of friction f between two sliding surfaces depends on the instantaneous slip rate as well as the past history of sliding [*Ruina*, 1983; *Marone*, 1998]. Following a step increase in sliding velocity, f immediately increases (the direct effect) but then decays exponentially (the evolution effect) over a characteristic distance scale d_c to a new steady state value. It is also observed that f increases roughly with the logarithm of time the surfaces are in static contact [*Dieterich*, 1972]. Although the variation in f is small, the effect may play an important role in earthquake nucleation and other fault processes [see *Marone*, 1998; *Segall*, 2010].

[31] Common formulations of rate- and state-dependent friction (section A4) are unphysical as velocity approaches zero, and therefore ill suited for modeling the waning phases of an eruption. *Rice et al.* [2001] derived a regularized expression based on the friction laws of *Dieterich* [1979] and *Ruina* [1983] which overcomes this limitation. Assuming for simplicity that there are no state evolution effects, which may be appropriate for high temperature sliding of granite surfaces [*Blanpied et al.*, 1998], solid plug shear tractions τ_p are equal to

$$\tau_p = a\overline{\sigma}\,\mathrm{arcsinh}\left(\frac{v}{2v_r}\exp\frac{f_0}{a}\right), \tag{11}$$

where v is sliding velocity, f_0 is the coefficient of friction at the reference sliding velocity v_r, a governs the direct effect, and $\overline{\sigma}$ is the mean effective normal stress (depth average of normal stress minus pore fluid pressure) on the sliding surfaces, calculated using

$$\overline{\sigma} = \sigma_c \rho_l g L/2, \tag{12}$$

where σ_c is a coefficient relating lithostatic pressure to normal stress on the plug. For a shallow conduit surrounded by cohesionless fallback material, with pore pressure ranging from 0 to the least compressive stress and $f_0 = 0.6$, *Mastin et al.* [2008] estimates $\sigma_c \approx 1/3$ to 3 times the vertical stress.

3.2. Magma Chamber

[32] Properties of magma in the chamber are averaged throughout, such that density, compressibility, and other parameters represent average values (however, the full chamber shape is used to calculate deformation). At the onset of the eruption the magma chamber has an initial volume V_0. We consider two chamber pressures: the pressure at the top of the chamber p_{ch} which drives flow into the conduit, and the pressure at the center of the chamber p_{cc}, which may be considered an 'average' chamber pressure, and is used to calculate magma compressibility. The magma in the chamber is parameterized by overpressure and initial volatile content at the top of the chamber and base of the conduit ($z = -L - L_c$). Pressure at the center of the chamber p_{cc} is calculated from p_{ch} assuming a magmastatic pressure gradient and, for simplicity, a constant average magma density of $\overline{\rho}_m = 2300$ kg/m^3.

[33] As an eruption progresses magma flows out of the chamber into the conduit; magma may also flow into the chamber from a deeper source. The rate of pressure change in the chamber dp_{ch}/dt depends on rates of volumetric outflux q_{out} and influx q_{in} into the chamber, as well as the compressibility β_{ch} of the chamber and the compressibility β_m of the magma within the chamber [e.g., *Segall et al.*, 2001]:

$$\frac{dp_{ch}}{dt} = \frac{q_{in} - q_{out}}{V_0(\beta_m + \beta_{ch})}. \tag{13}$$

Chamber outflux q_{out} is given by $\pi R^2 v_{ch}$ where v_{ch} is the velocity at the chamber/conduit interface. We estimate the chamber influx q_{in} by assuming that influx is driven by some deeper, constant pressure p_{deep}, such that influx is linearly proportional to drop in magma chamber pressure [e.g., *Mastin et al.*, 2008]:

$$q_{in} = \Omega\left(p_{deep} - p_{ch}\right), \tag{14}$$

where Ω is a scaling factor with units of volume flux per pressure difference.

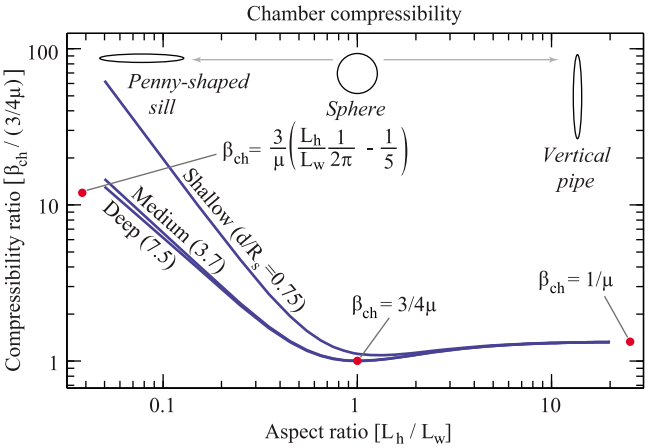

Figure 5. Finite element calculations of magma chamber compressibility β_{ch} as a function of aspect ratio $\omega = L_h/L_w$ in an elastic half-space, shown relative to the compressibility of a sphere in a full space $3/4\mu$. The volume of the chamber is kept constant and the top of the chamber at a fixed depth d; three depths are shown (normalized by the radius R_s of a sphere with an equivalent volume). Penny-shaped cracks (left) become highly compressible, while vertical pipe-like chambers (right) become only somewhat more compressible than the sphere. Analytical expressions and results from *Amoruso and Crescentini* [2009] are shown for a sphere, penny-shaped crack (with $\nu = 0.25$), and highly elongate vertical prolate ellipsoid (all in elastic full-spaces); the latter two are end-member cases so their horizontal position on the axes is approximate. Analytical approximations fail most significantly with shallow penny-shaped chambers.

[34] Compressibilities are defined as

$$\beta_m = \frac{1}{\rho_{cc}}\frac{\partial \rho_{cc}}{\partial p_{cc}}, \tag{15a}$$

$$\beta_{ch} = \frac{1}{V}\frac{\partial V}{\partial p_{cc}}, \tag{15b}$$

where ρ_{cc} is the bulk density of magma in the chamber at pressure p_{cc}. We evaluate $\partial\rho/\partial p$ using equation (3).

[35] The compressibility β_{ch} of the chamber itself is a function of its shape and depth. For a spherical chamber in an elastic full-space, $\beta_{ch} = 3/4\mu$ where μ is the shear modulus of the elastic medium [*McTigue*, 1987]; however, this result does not hold for nonspherical shapes [*Amoruso and Crescentini*, 2009]. Using the finite element method we numerically compute β_{ch} for chambers with aspect ratios ω ranging from 0.05 to 20 in an elastic half-space with $\nu = 0.25$ and $\mu = 20$ GPa. We find good agreement with full-space analytical results for the sphere, and the prolate spheroid and penny-shaped crack given by *Amoruso and Crescentini* [2009] for deep magma chambers (Figure 5). As the relative chamber depth decreases the numerical results begin to diverge from these analytical approximations, particularly for penny-shaped chambers. For deep prolate ellipsoids, $\beta_{ch} = 1/\mu$ [*Amoruso and Crescentini*, 2009], so errors using the spherical approximation ($\beta_{ch} = 3/4\mu$) will not exceed ~25%.

[36] For the inverse problem (in part 2), we precompute compressibility for a wide range of aspect ratios and chamber depths and interpolate between these results to find the appropriate β_{ch}.

4. Numerical Solution

[37] The final system of equations is strongly nonlinear. For initial conditions p_{ch_0}, V_0, ω, χ_d^w, etc., we solve the equations of magma ascent from $t = 0$ to the final time $t = t_f$ and then use the solution to calculate observables such as ground deformation (section 5).

[38] The governing system of equations, including expressions for momentum conservation, density, and mass conservation (equations (1), (3), and (2), respectively), is given by

$$\begin{bmatrix} 0 \\ 0 \\ \partial\rho/\partial t \end{bmatrix} = \begin{bmatrix} \partial p/\partial z + \rho g + 8\eta v/R^2 \\ \rho - \rho^* \\ -\partial(\rho v)/\partial z \end{bmatrix}, \tag{16}$$

where the explicit analytical expression for density ρ^* (which is an implicit function of pressure in equation (16)) is used as a constraint on the unknown ρ. Note that unknowns p, v, and ρ are functions of position z and time t; i.e., $\rho = \rho(z, t)$.

[39] The boundary condition at the top of the conduit is found by equating force balance on the plug (equation (10)) with rate-dependent shear tractions (equation (11)), which yields a relationship between plug velocity v_p and pressure at the base of the plug p_p. Solving for v_p yields the velocity boundary condition

$$v_p = \frac{2v_r}{\exp(f_0/a)}\sinh\left\{\frac{R\left[p_p - \rho_p(L+h)g\right]}{2La\bar{\sigma}}\right\}, \tag{17}$$

where p_p and ρ_p are both functions of time. The boundary condition at the bottom of the conduit is simply $p = p_{ch}$, which may be obtained using equations (13) and (14):

$$\frac{dp_{ch}}{dt} = \frac{\Omega\left(p_{deep} - p_{ch}\right) - \pi R^2 v_{ch}}{V_0(\beta_m + \beta_{ch})}, \tag{18}$$

and initial condition

$$p_{ch}(t = 0) = p_{ch_0}, \tag{19}$$

where v_{ch} and β_m are functions of time.

[40] Spatial derivatives along the conduit are approximated by discretizing in space and employing the finite difference operator **D**. For points away from the boundaries we use the fourth-order stencil

$$\partial f/\partial z \approx \mathbf{D}[f_j] = \left(f_{j-2} - 8f_{j-1} + 8f_{j+1} - f_{j+2}\right)/(12\Delta z), \tag{20}$$

where $j = 1,2, \ldots, n-1$, such that $j = 0$ would correspond to the magma chamber and $j = n$ to the plug, and Δz is the (constant) discretization spacing. Lower-order finite difference operators are used as necessary near the boundaries.

[41] We do not attempt to model the onset of the eruption, but rather assume that at $t = 0$ the flow rate has already reached its maximum value and define initial conditions at this time (these values should not differ significantly from preeruption values if the onset was relatively rapid). To do so we solve the steady state version of equation (16) for

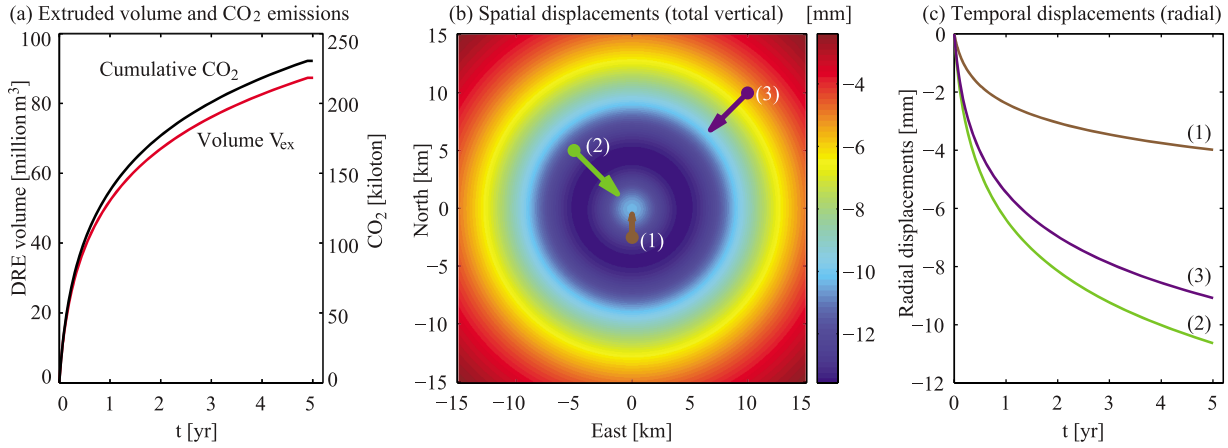

Figure 6. Some of the types of observables predicted by the model, here using nominal parameters. (a) Extruded volume time series (which can be compared to dome growth time series), and cumulative CO_2 emissions. The two curves are identical in shape (although scaled slightly differently here) because CO_2 emissions are calculated directly from extruded volume time series. (b) The spatial pattern of total vertical displacements, similar to what might be recorded by InSAR. Deformation calculated using *Yang et al.* [1988]. (c) Temporal deformation time series (radial) for points shown in Figure 6b, similar to what might be recorded by GPS.

initial values $p_j(t = 0)$, $v_j(t = 0)$, and $\rho_j(t = 0)$, and then time step the full system of equations

$$\begin{bmatrix} 0 \\ 0 \\ d\rho_j/\partial t \\ dp_0/dt \end{bmatrix} = \begin{bmatrix} \mathbf{D}[p_j] + \rho_j g + 8\eta_j v_j/R^2 \\ \rho_j - \rho_j^* \\ -\mathbf{D}[\rho_j v_j] \\ \left[\Omega\left(p_{deep} - p_0\right) - \pi R^2 v_1\right]/V_0(\beta_m + \beta_{ch}) \end{bmatrix} \quad (21)$$

with boundary condition given by

$$v_n = \frac{2v_r}{\exp(f_0/a)} \sinh\left\{\frac{R[p_n - \rho_n(L+h)g]}{2La\bar{\sigma}}\right\} \quad (22)$$

and initial condition

$$p_0(t = 0) = p_{ch_0}. \quad (23)$$

(Note that v_n in equation (22) is coupled to the system in equation (21) through the $\mathbf{D}[\rho_j v_j]$ term, which includes v_n at the top of the fluid conduit.) This system is a Differential-Algebraic Equation (DAE) with independent variable t for unknowns $p_j(t)$, $v_j(t)$, $\rho_j(t)$, and $p_0(t)$, which we time step using a MATLAB ODE solver (ode15s) suitable for DAEs. To verify the system of equations and numerical procedures under certain limiting assumptions, we compare results to an analytical model by *Mastin et al.* [2008] (see section A5).

[42] Posteruptive periods ($t > t_f$) may be modeled by constraining conduit velocity to zero and solving the simplified system of equations. This formulation allows chamber recharge due to continued influx from a deeper source, leading to a pressure increase and a deformation signal in the absence of conduit flow.

5. Calculation of Observables

[43] Extruded volume V_{ex} is obtained by integrating the volume flux at the top of the conduit and removing bubble volume fraction α^v to obtain the dense rock–equivalent (DRE) volume (Figure 6a).

[44] Time-dependent carbon dioxide emissions may be approximated by assuming that the CO_2 flux equals the CO_2 mass fraction times the mass flux of liquid (nonphenocryst) magma [e.g., *Gerlach et al.*, 2008] (Figure 6a).

[45] Time-dependent ground displacements $u(\mathbf{x}, t)$ are calculated at position $\mathbf{x}$ on the surface due to changes in chamber and conduit pressures $p_{cc}(t)$ and $p(z, t)$, respectively, and shear tractions $\tau(z, t)$ and $\tau_p(z, t)$ for the fluid conduit and solid plug, respectively, using

$$u(\mathbf{x}, t) = u_{cc}(p_{cc}) + u_p(p) + u_\tau(\tau, \tau_p), \quad (24)$$

where u_{cc}, u_p, and u_τ are functions which give displacements due to the evolving chamber pressure, conduit pressures, and conduit shear tractions, respectively.

[46] Pressures p and p_{cc} are available directly from the solution to equations (21)–(23). Tractions $\tau_p(t)$ generated by the solid plug are calculated using equation (11). Shear tractions $\tau(z, t)$ in the fluid conduit are obtained by integrating the equilibrium equations in cylindrical coordinates under conditions of radial symmetry, $\partial(r\sigma_{rz})/\partial r + r\partial(\sigma_{zz})/\partial z = 0$ [e.g., *Segall*, 2010], then substituting using equation (1) to obtain

$$\tau(z, t) = 4\eta v/R, \quad (25)$$

where τ acts in the direction opposite to flow.

[47] Analytical models exist for u_{cc} [*Mogi*, 1958; *Yang et al.*, 1988], u_p [*Bonaccorso and Davis*, 1999], and u_τ [*Nishimura*, 2009; K. Anderson and P. Segall, Ground deformation associated with volcanic conduits, manuscript in preparation, 2011]. Although computationally inexpensive, these models rely on various assumptions and do not easily allow for spatial variations in material properties or topography. On the other hand, numerical techniques allow for the inclusion of an arbitrary degree of realism including

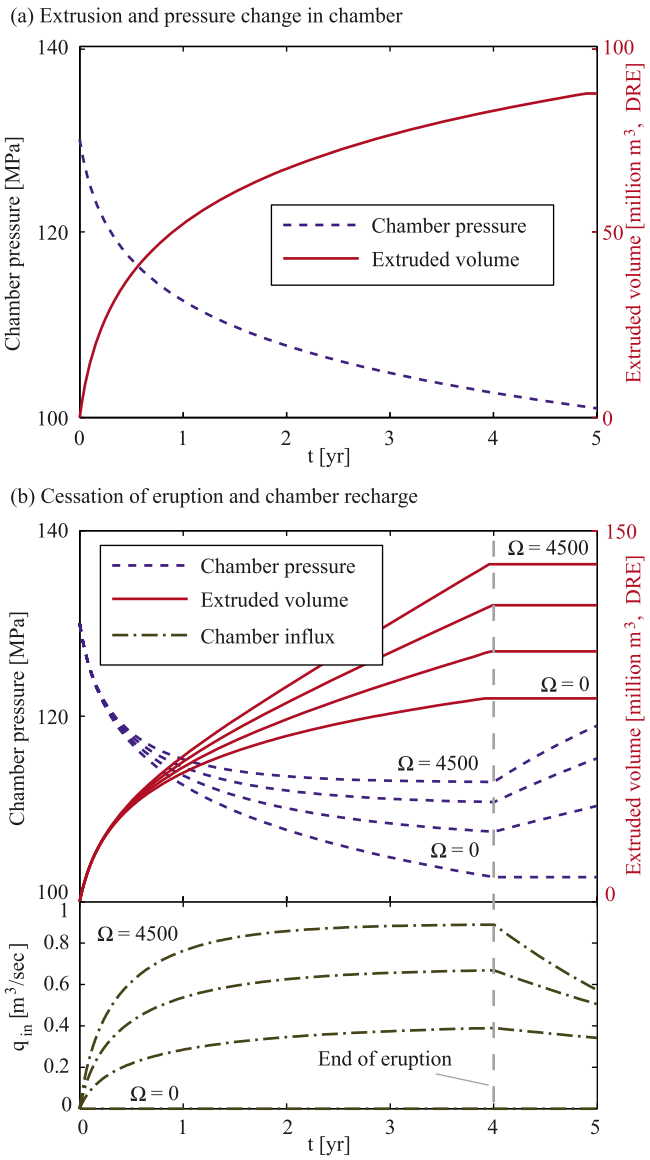

Figure 7. Magma chamber pressure (dashed lines) and extruded volume (solid lines) with time for the nominal model parameters. (a) Evolution without influx into the chamber. Without forced termination, the eruption would continue at a decreasing rate for decades. (b) The same eruption with termination at 4 years, and the addition of chamber recharge using Ω = [0, 1500, 3000, 4500] m^3 day^{-1} MPa^{-1}. Addition of recharge alters time series during the eruption and leads to chamber reinflation after the cessation of the eruption. Repressurization occurs at a decaying rate such that chamber pressure will eventually recover p_{ch_0}. For the highest value of Ω, influx rates approach 1 m^3/sec late in the eruption.

complex surface topography and layering of earth properties, but can be slower to compute.

[48] We precompute influence functions G using radially symmetric topography (future work may include full three-dimensional topography for individual volcanoes). Influence functions are dependent on receiver position $\mathbf{x}$ and source properties which include chamber aspect ratio ω, chamber volume V_0, and conduit length L. After equation (24), deformation is then calculated using

$$u(\mathbf{x},t) = G^p_{cc}(\mathbf{x}, L+L_c\omega, V_0)p_{cc}(t) + \sum_j G^p_j(\mathbf{x}, z_j, R)p_j(t) + \sum_j G^\tau_j(\mathbf{x}, z_j, R)\tau_j(t) + G^{\tau_p}_{plug}(\mathbf{x}, R)\tau_p(t), \quad (26)$$

where G^p_{cc}, G^p_j, G^τ_j, and $G^{\tau_p}_{plug}$ are influence functions associated with chamber pressure, fluid conduit pressures, fluid conduit tractions, and sliding plug tractions, respectively, and j is the conduit discretization as defined in section 4. Once functions G are precomputed, this approach yields the speed of an analytical method with the realism and flexibility of a numerical approach (computational speed becomes important when running many forward models, as in the Monte Carlo inversion procedure we follow in part 2).

[49] The resulting deformation field is fully characterized in space (Figure 6b) and time (Figure 6c) and may be compared to InSAR, GPS, tilt, and other data.

[50] For nominal eruption parameters described in section 6.1, we find that displacements due to the conduit are small relative to displacements due to the chamber except for observations made close to the conduit. The fluid conduit, in particular, generates relatively little ground deformation although at closer distances the influence of the solid plug can become significant. A more detailed analysis of ground deformations generated by the conduit, including the solid plug, will be examined in future work; for the remainder of this study we focus on deformations generated by the chamber.

6. Model Behavior

[51] We examine model behavior using a set of nominal parameter values given in Table 1. These values should be generally appropriate for effusive silicic eruptions, but are not meant to represent a particular volcano. We show results both with and without a forced cessation of the eruption at t_f = 4 years.

6.1. Solution With Nominal Parameters

[52] After 5 years, the nominal eruption yields an extruded DRE volume of about 87 million m^3, and chamber pressure is reduced by 29 MPa (Figure 7a). With a friction law dependent only on slip rate, the eruption continues for many years with monotonically decreasing extrusion rate; after 200 years, extrusion rate has dropped to 0.003 m^3/sec from more than 9 m^3/sec at the onset of the eruption. A more realistic friction law would cause the plug to lock up and terminate the eruption (as would a more realistic consideration of crystallization), but we postpone such an analysis to a future study, and here impose an end to the eruption at a fixed time (Figure 7b).

[53] The ability to simulate posteruptive periods is an important feature of the model, as geodetic evidence for reinflation can provide a valuable constraint on chamber recharge which is difficult to estimate during an eruption. Figure 7b shows the nominal eruption including chamber recharge. For an eruption involving no precursory inflation we set $p_{deep} = p_{ch_0}$ (see equation (14)) so that $q_{in}(t = 0) = 0$, and examine the effect of different values of Ω. Recharge

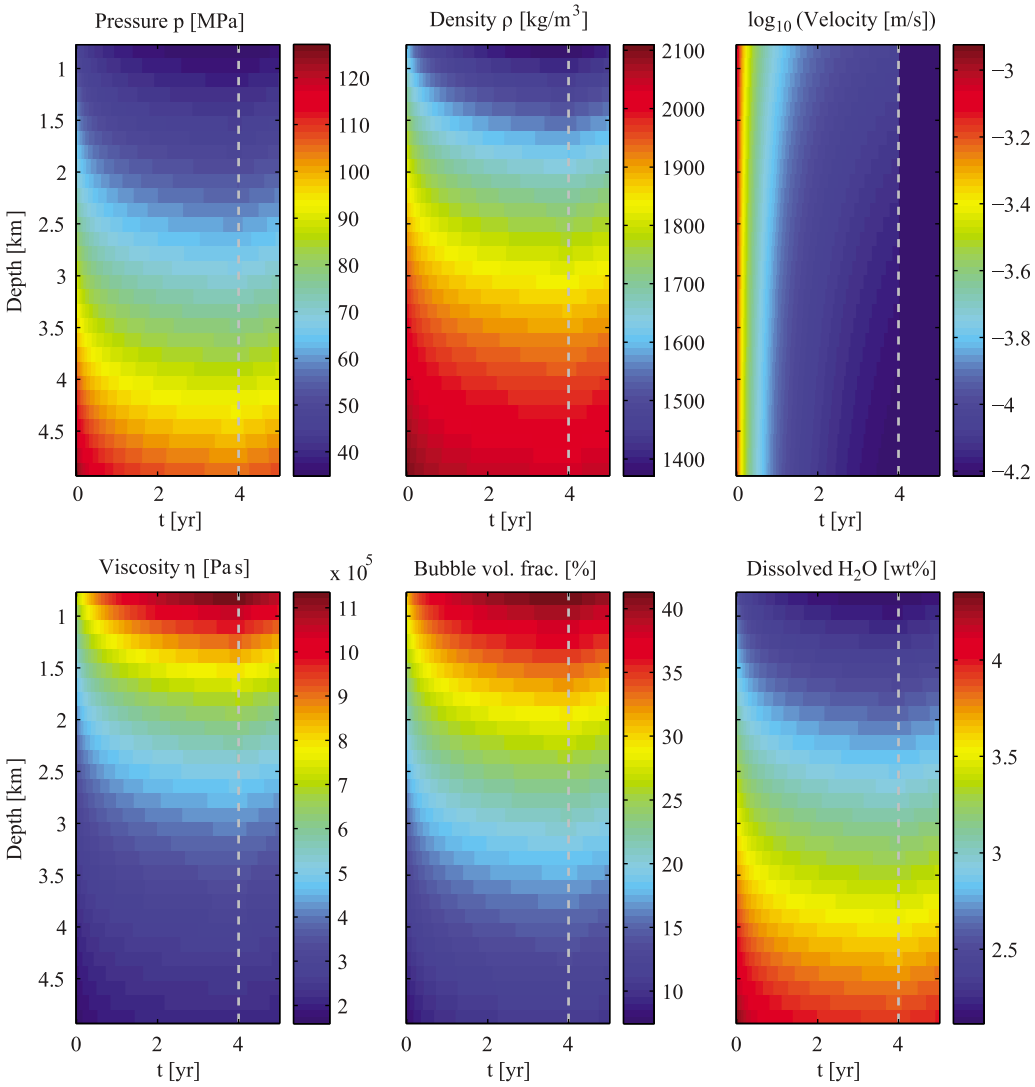

Figure 8. Evolution of magma properties in the conduit using nominal model parameters, with Ω = 1500 m^3 day^{-1} MPa^{-1} and with forced cessation at t = 4 years (vertical dashed line). Pressure, density, velocity and dissolved water all decrease throughout the eruption, while viscosity and bubble volume fraction increase; these trends reverse and velocity drops to zero during chamber repressurization following the end of the eruption.

causes the extrusion rate to approach a constant value, and the magma chamber pressure to decay more slowly. Reinflation of the chamber following the eruption occurs at a decaying rate such that chamber pressure eventually recovers p_{ch_0}.

[54] Depth- and time-dependent variation in magma properties in the conduit are shown in Figure 8, with Ω = 1500 m^3 day^{-1} MPa^{-1} and with t_f = 4 years. Bubble volume fraction varies from <10% at the top of the chamber to ~40% at the base of the plug, suggesting that gas loss is probably not significant for most of the conduit with these parameters. After the end of the eruption, repressurization due to chamber recharge can be seen, causing exsolved gas to reenter solution in the magma, and an increase in magma density.

[55] Although a fit to specific data is not the focus of this work (see instead part 2), to demonstrate that the model is capable of recovering the general characteristics of an actual eruption we compare to the 2004–2008 eruption of Mount St. Helens, Washington, using a representative set of model parameters. These parameters are somewhat different than the nominal set, including a larger chamber of ~25 km^3. (They should not be considered "best fitting" parameters; in part 2 we invert the observations from this eruption to find posterior probability density functions of the model parameters using a Markov Chain Monte Carlo approach.)

[56] Figure 9 shows the fit of this tentative model to dome growth and GPS time series at Mount St. Helens, where to match observations we constrain the model extrusion velocity to 0 at the end of the eruption in January 2008 after ~3.3 years. The model fits the general characteristics of both the GPS and dome growth data, although the fit is imperfect and does not explain apparent posteruptive inflation at the volcano. These issues are treated in detail in part 2.

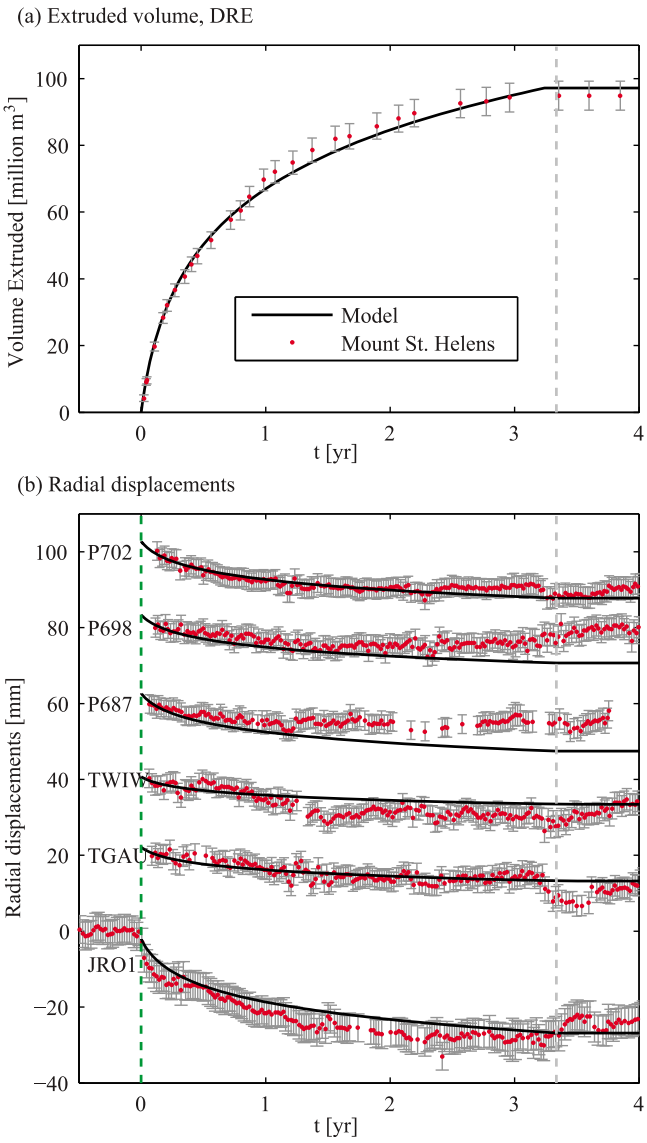

Figure 9. Comparison of model to data from the 2004–2008 eruption of Mount St. Helens. This result is not intended to show the best fitting model; for an in-depth study on fitting this data, see part 2. Cessation of the eruption is forced at the vertical gray dashed line (to fit observations). (a) Growth of the lava dome versus time. Final posteruption data points are based on seismic, gas, and geodetic evidence suggesting the cessation of extrusion, not on dome volume estimates. (b) Continuous weekly GPS time series, radial from the volcano (see *Lisowski et al.* [2008] for information about the GPS network). Uncertainties shown are for daily solutions (white noise only). Model at JRO1 is offset by 2 mm to account for the time difference between the onset of ground deformation and measurable extrusion.

6.2. Influence of Parameters on Observables

[57] We examine how model parameters influence two key observables: volume extruded V_{ex} and $\tilde{u} \equiv V_0 \Delta p_{ch}$, the latter being proportional to ground displacements when the dimensions of the chamber are small compared to its depth. We also examine how vesicularity α^v, magma compressibility β_m, and the importance of time-dependent terms in the solution (section 6.6) vary with these same model parameters. Simulations are run until the approximate cessation of an eruption ($v \to 0$). Results represent parameter-by-parameter deviations from the nominal model parameters, not accounting for correlations between parameters. Results are therefore strictly valid only in the region of the nominal model.

[58] Figure 10a shows the temporal evolution of observables V_{ex} and $\tilde{u}$ with variations in nine key model parameters, with dashed lines connecting points at which V_{ex}/V_f and $\tilde{u}/\tilde{u}_f$ reach $1 - 1/e \approx 0.63$ (defining a time constant), where the subscript $_f$ indicates the final value at the end of the eruption and we use the DRE estimate for V_f. All examined model parameters influence the time constant t_c, while some also influence V_f and total displacements $\tilde{u}_f$ (not generally visible in these plots which end at $t = 20$ years). Erupted volume increases more rapidly with larger V_0 and R, as expected. Interestingly, the extruded volume increases with the volatile concentrations (χ_d^w and χ_T^c), but displacements show a weaker dependence. It can also be seen that the effect of p_{ch_0} on volatile solubility (and hence magma compressibility) overwhelms the expected behavior that larger p_{ch_0} produces more erupted magma.

[59] To examine these and other dependencies more closely, in the first two rows of Figure 10b we plot t_c, V_f, and $\tilde{u}_f$ as functions of the same key model parameters. Results confirm that all parameters influence the time constant t_c, but (due largely to the compressibility of the magma) V_{ex} and $\tilde{u}$ exhibit different t_c; this is in contrast to a simple analytical model of a deflating magma chamber which predicts identical t_c given by (section A5)

$$t_c = 8\overline{\eta} L_c V_0 (\beta_m + \beta_{ch})/\pi R^4, \tag{27}$$

where β_m is assumed constant in time and $\overline{\eta}$ indicates the depth-averaged viscosity, also constant in time.

[60] Equation (27) predicts that t_c should vary linearly with V_0 and inverse quartically with R. These predictions are shown as black lines in Figure 10b (scaled to match numerical results as closely as possible); agreement is good for R and poor for V_0, in part because V_0 influences the depth of the center of the chamber, which influences the exsolved gas fraction and thus compressibiltiy β_m in equation (27). This dependency leads to nonlinear scaling of t_c with V_0.

[61] Sensitivity of t_c to frictional parameters σ_c, f_0, and a cannot be predicted using analytical approximations which do not include a frictional plug, but some inferences may be made by examination of the unregularized rate-dependent friction law (equation (A9)). It is clear that larger σ_c (which controls $\overline{\sigma}$; see equation (12)), L, and f_0 increase the net plug frictional resistance and therefore reduce effusion rate and increase t_c. The regularized version of the expression (equation (11)) shows that friction scales with $a\overline{\sigma}$ and f_0/a. Numerical results show that larger values of a actually decrease t_c by increasing the time dependence of friction, suggesting that f_0/a dominates.

[62] Total extruded volume V_f and final displacements $\tilde{u}_f$ at the end of the eruption are particularly sensitive to V_0

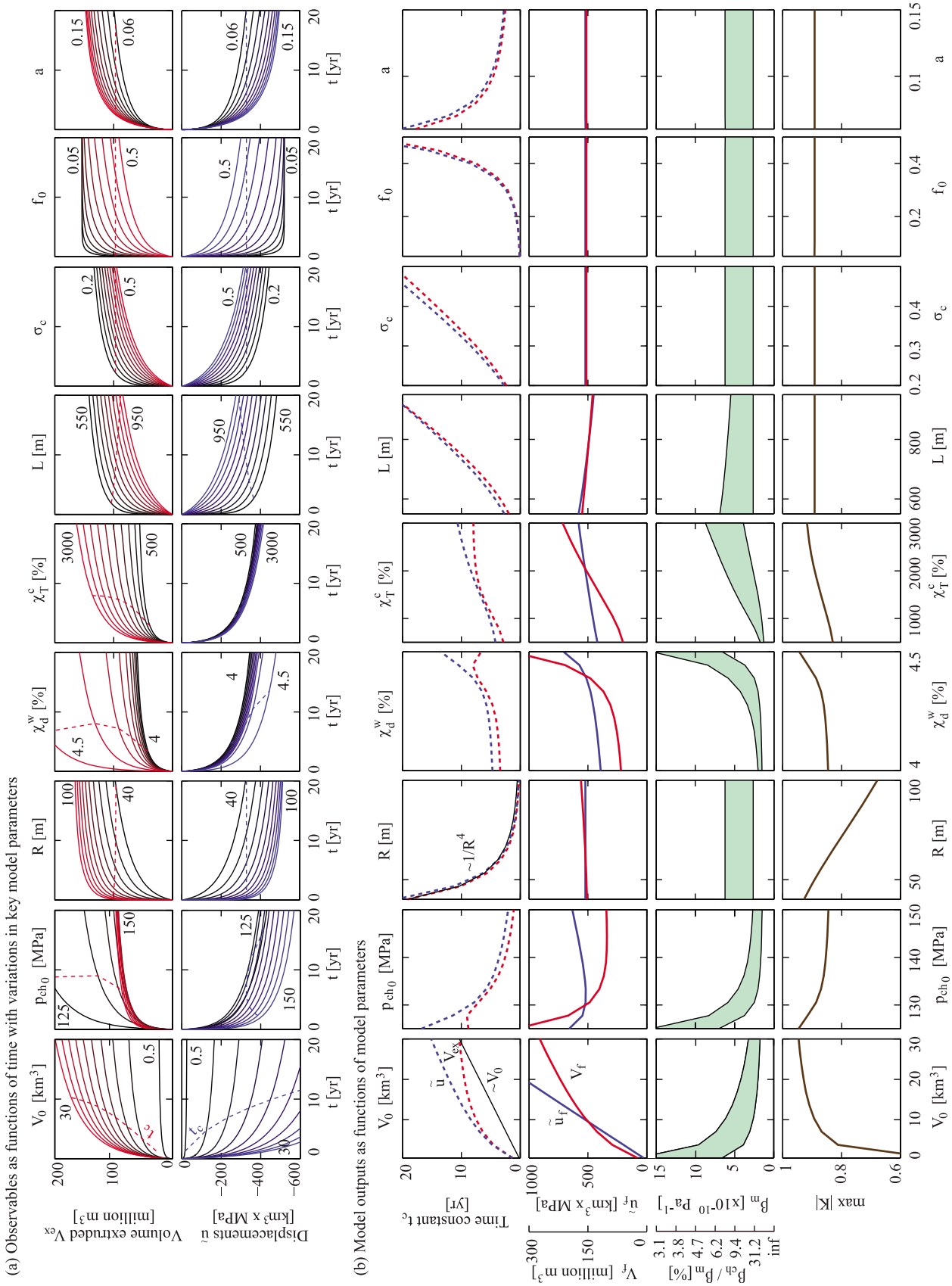
(a) Observables as functions of time with variations in key model parameters
Volume extruded V_{ex} [million m^3]
Displacements $\tilde{u}$ [km^3 x MPa]
(b) Model outputs as functions of model parameters
Time constant t_c [yr]
$\tilde{u}_f$ [km^3 x MPa]
V_f [million m^3]
β_{ch} / β_m [%]
β_m [x10^{-10} Pa^{-1}]
max |K|
V_0 [km^3]
p_{ch0} [MPa]
R [m]
χ_d^w [%]
χ_T^c [%]
L [m]
σ_c
f_0
a
t [yr]
~1/R^4
~V_0
V_{ex}
V_f
$\tilde{u}$
$\tilde{u}_f$
t_c

Figure 10

and p_{ch_0}, as predicted in the analytical approximations $\tilde{u}_f = V_0\Delta p_f = V_0(\overline{\rho}gL_c - p_{ch_0})$ and $V_f = -V_0(\overline{\beta}_m + \beta_{ch})(\overline{\rho}gL_c - p_{ch_0})$ (see section A5). Dependence on p_{ch_0} is somewhat counterintuitive, with a minimum in $\tilde{u}_f$ at around 130 MPa, and larger p_{ch_0} leading to smaller V_f. This behavior is due to the way we define dissolved water content at p_{ch_0}, which leads to very high total water content and magma compressibility near the solubility limit at ~125 MPa. V_f also shows a very strong dependency on volatile concentration χ_d^w (and to a less exstent on χ_T^c); this is because increasing χ_d^w from 4% to 4.5% at 130 MPa increases the total H_20 content χ_T^w by more than a factor of two, leading to a large increase in compressibility and thus V_f. No dependence of $\tilde{u}_f$ or V_f on plug friction parameters is observed because the model for plug friction includes no locking strength (as $v \to 0$, $\tau \to 0$ in equation (11)). Inclusion of a frictional plug therefore influences the evolution of an eruption, but not its final outcome (except to the relatively minor extent that plug density is different from melt density).

[63] For the parameters explored, bubble fractions α^v at the top of the conduit during an eruption typically range from 30% or less at the onset to more than 50% at the end of the eruption due to decreased conduit pressure. Values at the top of the conduit are mostly lower than the critical bubble fraction (percolation threshold) required for significant permeability in some studies [e.g., *Eichelberger*, 1995; *Takeuchi et al.*, 2005], but not in other studies which suggest relatively high permeabilities even at low porosities [e.g., *Klug and Cashman*, 1996; *Melnik and Sparks*, 2002], perhaps due to the presence of crystals [*Collombet*, 2009]. These results suggest that the assumption of no conduit outgassing is probably appropriate for most of the fluid conduit (where bubble fractions are modest), but the assumption may be less valid at shallow depth for late in eruptions with gas-rich melts.

6.3. Chamber Compressibility and Host Rock Rigidity

[64] The compressibilities β_m and β_{ch} of the magma and chamber, respectively, are an important control on eruption duration and volume. While early work considered primarily the elastic compressibility of the host rock surrounding the chamber [*Stasiuk et al.*, 1993], more recent work has suggested that the compressibility of the magma plays a dominant role due to the high compressibility of the exsolved gas phase [*Huppert and Woods*, 2002; *Melnik and Sparks*, 2005].

[65] These conclusions rest on estimates of β_m and β_{ch}. For a homogeneous medium, β_{ch} is inversely proportional to shear modulus μ. Shear modulus may be only poorly known because static elastic modulii can be appreciably less then those inferred from seismic wave speeds [e.g., *Lin and Heuze*, 1987], and the presence of fractures in situ can further reduce stiffness relative to laboratory tests. In part due to these fractures, μ may vary greatly: for fractured rocks or sediments μ may be <1 GPa, while for more competent rocks $\mu > 30$ GPa [e.g., *Dzurisin*, 2007, p. 281]. As a result, β_{ch} may be very poorly constrained. (For a linear, homogenous elastic medium, ground displacements scale linearly with shear modulus, so the uncertainty in μ also plays an important role in interpreting this observable.)

[66] The compressibility of magma in the chamber β_m may also vary considerably with volatile content (and parameters which influence volatile content) and change throughout an eruption. Figure 10b shows maximum values of β_m sometimes exceeding 15×10^{-10} Pa^{-1} at the end of an eruption (top of shaded region), while minimum values for the onset of an eruption (bottom of the shaded region) are often $<3 \times 10^{-10}$ Pa^{-1}. Compressibility β_m increases significantly with higher volatile concentrations, smaller V_0 (because larger chambers extend to deeper depths and contain less compressible magma) and with smaller p_{ch_0} (because lower pressures increase total dissolved water, as noted in section 6.2). For $\mu = 20$ GPa and $\beta_{ch} = 4.7 \times 10^{-11}$ Pa^{-1} (section 3.2), β_{ch} varies between <3% and >30% of β_m, suggesting that chamber compressibility could be an important effect and should not be neglected.

6.4. Volume Change of Magma Chamber

[67] Geodetic estimates of total volume change ΔV_{ch} in a magma chamber are commonly smaller than the volume of magma V_f extruded onto the surface, or the estimated volume of intruded dikes [*Owen et al.*, 2000; *Wright et al.*, 2006; *Lisowski et al.*, 2008]. While such differences have been attributed to chamber recharge from a deeper, geodetically invisible source, they may sometimes be explained by compressibility of the melt and of the magma chamber as shown in the relationship $V_f/\Delta V_{ch} = -(1 + \beta_m/\beta_{ch})$ [e.g., *Mastin et al.*, 2008; *Rivalta and Segall*, 2008; *Segall*, 2010], which demonstrates that $V_f = \Delta V_{ch}$ only when the magma is incompressible.

[68] We calculate the ratio $V_f/\Delta V_{ch}$ for the parameter combinations explored in Figure 10. Results generally follow compressibility relationships shown in Figure 10b because higher values of β_m lead to larger (more negative) $V_f/\Delta V_{ch}$. As a result, the magnitude of $V_f/\Delta V_{ch}$ increases significantly with higher volatile concentrations and decreases strongly with larger V_0 and p_{ch_0}. For the nominal parameters, the ratio is around −6, but with different parameters ranges from roughly −3 to −20. These results, which explore only a small part of parameter space, are not

Figure 10. Dependence of model behavior on key model parameters (arranged by column). (a) Time series (solid lines) of observables as functions of different model parameters, with colors (red for V_{ex} and blue for $\tilde{u}$) indicating large parameter values and black lines indicating small parameter values (minimum and maximum curves are also labeled). Dashed lines connect points at which the observable reaches ~63% of its final value (t_c). (b) First row shows time constants t_c calculated from results in Figure 10a, some with comparison to analytical results (see text). Second row shows final extruded DRE volume V_f and "displacements" $\tilde{u}_f$. Third row shows magma compressibility in the chamber β_m, with the shaded region indicating the range between minimum ($t = 0$) and maximum ($t = t_f$) values during a given eruption; for example, β_m varies between roughly 2.6×10^{-10} Pa^{-1} and 6.2×10^{-10} Pa^{-1} for $V_0 = 10$ km^3. Fourth row shows maximum value of $|K|$ in the conduit during the eruption (section 6.6), where smaller values indicate increasing importance of time-dependent terms.

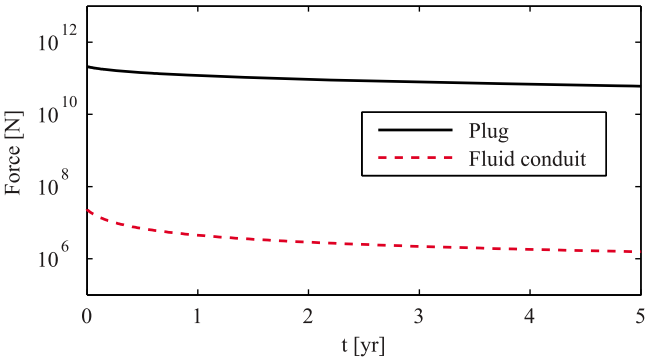

Figure 11. Total resistive forces generated by the solid plug and the fluid (Newtonian) conduit for the nominal set of eruption parameters. The force generated by the plug is orders of magnitude higher than that generated by the conduit.

inconsistent with the estimated $V_f/\Delta V_{ch}$ ratio at Mount St. Helens of around −3 to −5 [*Lisowski et al.*, 2008; *Mastin et al.*, 2009] (and results in section 6.1 show that with appropriate parameters these results can be reproduced). Results confirm that magma and chamber compressibilities may explain excess erupted volumes without requiring magma chamber recharge.

6.5. Conduit Force Balance

[69] For the nominal eruption parameters, Newtonian viscosities below the solid plug are relatively low and pressure gradients are nearly constant. Because of the low viscosity, the fluid part of the conduit plays an insignificant role in the overall momentum balance and eruption dynamics are dominated by the competition between magma chamber pressure and frictional plug resistance (Figure 11).

[70] These results can be quantified in a simple way by taking the ratio of resistive forces exerted by the solid plug ($2\pi RL\tau_p$) to resistive forces exerted by the fluid conduit (equation (25) times $2\pi RL_c$) to obtain a nondimensional parameter which measures the ratio of frictional to viscous forces:

$$\psi = \frac{RL\tau_p}{4L_c\overline{\eta}\,\overline{v}}. \tag{28}$$

Using the nominal model parameters and solution at $t = 0$ ($\tau_p \approx 1 \times 10^6$ Pa and $\overline{v} \approx 1 \times 10^{-3}$ m/s), forces achieve parity ($\psi = 1$) for $\overline{\eta} \approx 2 \times 10^9$ Pa·s, which is more than four orders of magnitude higher than the viscosities calculated in the nominal eruption.

[71] Since average viscosity increases nonlinearly as the plug is shortened and Newtonian flow extends to shallower depths, is there a point at which $\overline{\eta} \to 2 \times 10^9$ Pa·s and $\psi \to 1$? *Sparks* [1997] calculates $\overline{\eta}$ for several models involving Newtonian ascent to the surface with no frictional plug, and $\overline{\eta}$ does not much exceed $\overline{\eta} = 1 \times 10^8$ Pa·s. The effect of crystal growth and other rheological changes as the fluid melt undergoes the transition to a solid state must greatly increase the melt viscosity in the transition zone just beneath the solid plug, but would probably not extend into the deeper conduit. Therefore, it seems likely that for typical silicic melt viscosities, upper conduit (solid plug + transition zone) forces most likely dominate viscous drag forces in the remainder of the conduit, except perhaps for systems with very shallow plugs, or possibly for gas-poor or crystal-rich magmas.

6.6. Importance of Time-Dependent Terms

[72] The importance of time-dependent terms in the solution may be evaluated by expanding the right-hand side of the continuity equation (equation (2)) and taking the ratio K of the two terms:

$$K = \left(v\frac{\partial \rho}{\partial z}\right) / \left(\rho\frac{\partial v}{\partial z}\right). \tag{29}$$

The closer $|K|$ to 1, the less significant the $\partial\rho/\partial t$ term in the solution. For the nominal parameter values, $\partial\rho/\partial t$ terms are most important at the beginning of the eruption. For modest deviations from the nominal model parameters $|K|$ is typically not much less than 0.9, but very small magma chambers or wide conduits (which reduce ascent rates for a given volume flux) result in $|K| < 0.7$ or 0.6 (Figure 10b). The error introduced by making a quasi steady state assumption (a steady state conduit driven by a time-dependent boundary condition dp_{ch}/dt) would therefore depend on the model parameters chosen, and could vary from relatively minor to significant.

7. Discussion: Simplicity Versus Realism

[73] Simplification of any model provides obvious benefits, while additional complexity provides more realism. The balloon-and-straw model geometry is an obvious simplification. The assumption of constant conduit radius R may be valid for a conduit but less so for a more compressible dike, in which case there could be considerable feedback between pressure and cross section. However, while magma transport is likely to initiate in the form of dikes, long-lived eruptions, such as at Mount St. Helens, are likely to evolve to more axisymmetric conduits.

[74] The inclusion of a solid plug in the upper conduit matches observations at many volcanoes, plays an important role in eruption dynamics, and simplifies numerical analysis by removing extreme nonlinearities in nominally fluid properties in the shallow subsurface which occur due to greatly reduced volatile solubility and consequent crystallization at low pressures. Beneath the plug, gradients in pressure and other magma properties are nearly constant, and could in principle be approximated with depth-averaged values; this would allow us to replace $\partial p/\partial z$ in the momentum balance with $(p_p - p_{ch})/L_c$ (see section A5). However, this approach restricts the model to relatively deep plugs (pressure gradients beneath very shallow plugs would not be constant) and reduces our ability to carefully propagate observables upwards from the chamber.

[75] The friction law used for the margins of the plug is based on well-established experimental evidence, but usually at conditions far removed from those in the conduit. A simple linearly rate-dependent law might conceivably be used to capture the essential elements of rate-dependent friction with less complexity. On the other hand, adding state dependence to the friction model might allow us to more carefully consider the effect of the plug at the onset and cessation of the eruption.

[76] Results suggest that for typical effusive silicic eruptions, neglecting time-dependent terms in the continuity

equation could introduce a modest loss in accuracy and would also prevent future consideration of time-dependent conduit processes such as crystallization.

[77] Modeling gas loss in the lower conduit may be relatively unimportant due to low magma permeability, but more careful consideration of gas loss in the upper conduit will need to be considered in future work. A more detailed simulation of the processes involved in plug formation, explicitly including crystallization, would add realism and might allow for the analysis of oscillatory behavior, and will be considered in future work. However, inclusion of such processes in the model could add considerably complexity.

8. Conclusions

[78] Physics-based models of volcanic eruptions show great promise for their ability to predict multiple types of observables and thereby better constrain important properties of volcanic systems. Kinematic models of ground deformation, although useful, do not have predictive capability, cannot easily model additional data sets such as extrusion rate, gravity change, or gas emissions, and cannot in isolation uniquely estimate both the volume of a magma chamber and its pressure change [e.g., *McTigue*, 1987].

[79] The model developed in this study has the ability to predict the evolution of a gradually declining effusive eruption using realistic magma physics given appropriate material parameters and initial conditions. We use it to calculate two key observables, extruded volume and ground deformations as a function of time, along with a simplistic estimate of CO_2 emissions (directly proportional to extruded volume) and the dependence of these observables on initial conditions. The model can be extended in a straightforward manner to predict additional data sets such as gravity changes.

[80] Key features of the model include the ability to simulate posteruptive periods to better constrain chamber influx, inclusion of a rigid plug in the upper conduit with a regularized rate-dependent friction law, and time-dependent ground deformation calculated for an arbitrarily realistic medium as a function of overpressures and tractions acting on the chamber and conduit using precalculated Green's functions. However, because the focus of this work is the development of a relatively simple model capable of fitting geophysical time series within a modest solution time, we do not attempt to incorporate all possible physical-chemical processes in an erupting magma and the model is significantly simplified relative to some models of conduit flow [e.g., *Melnik and Sparks*, 2005].

[81] Results suggest that while important physical processes occur in the fluid conduit, it may be difficult to detect geophysically and that it contributes little to the total force balance governing the evolution of an eruption; effusive eruptions may therefore be dominated by the balance between overpressure in the magma chamber driving upward flow, and resistance in the upper conduit provided by frictional plug slip (and also probably the flow of highly crystalline near-solid magma just beneath the solid plug, although this is not modeled in this study). We observe that, for nominal parameters, the magma chamber compressibility is a significant ~15% of magma compressibility, although results are strongly dependent on host rock rigidity. Somewhat counterintuitively, plug friction parameters influence the evolution of an eruption but have no effect on the final erupted volume or pressure change in the magma chamber (this would not be true with state-dependent friction). Importantly, modeling posteruption reinflation may provide valuable constraints on influx into the magma chamber from a deeper source, but such influx is in general not necessary to explain observed differences between extruded volume and apparent source volume change: consistent with earlier studies, we find that large differences may be explained by compressibility of magma and chamber.

[82] Much work remains to be done before physics-based models of this type can be easily or routinely used for geophysical inversions. The continuation of this work in part 2 examines some of these techniques, and employs the forward model explored here to invert data from the 2004–2008 eruption of Mount St. Helens, Washington.

Appendix A

A1. Momentum Balance

[83] The well-known momentum balance equation for laminar fluid flow in a long, thin, vertical cylindrical pipe may be derived from the Navier-Stokes equations by assuming a no-slip boundary condition on the walls of the pipe, no horizontal variation in melt viscosity or density, and assuming that vertical derivatives of vertical velocity are negligible compared to horizontal derivatives of vertical velocity. Laminar flow is justified at low Reynolds numbers ($R_e < 2000$), where flow is dominated by viscous forces. Using $R_e = L_c q\rho/\pi R^2\eta$, for $\rho = 2000$ kg/m^3 magma with viscosity of $\eta = 10^6$ Pa·s flowing through a $L_c = 5$ km fluid conduit of radius $R = 50$ m, $Re = 2000$ corresponds to a flowrate of ~1.5×10^6 m^3/sec, which is many orders of magnitude above that expected during an effusive eruption.

[84] Under these assumptions, the momentum balance is given by [e.g., *Jaupart and Tait*, 1990]

$$0 = \frac{\partial p}{\partial z} + \rho g + \frac{8\eta v}{R^2}. \tag{A1}$$

The pressure gradient which drives flow is balanced by the weight of the magma and the viscous resistance to flow.

A2. Mass and Volume Fractions and Concentrations

[85] We use the terms mass fraction and volume fraction to refer to masses and volumes of individual phases normalized to the bulk magma, and the terms mass concentration and volume concentration to refer to masses and volumes of individual phases normalized to other phases (not necessarily the total bulk magma). Such concepts are simple, yet easily confused. To convert from mass fractions (α, c) to mass concentrations (χ_e, χ_d) we use

$$\chi_e = \alpha/\lambda \tag{A2a}$$

$$\chi_d = c/\lambda. \tag{A2b}$$

To convert from mass fractions to volume fractions we use

$$i^v = i\rho/\rho_i, \qquad \text{for} \quad i = \alpha, \phi, \lambda, c \tag{A3}$$

where the ^{v} superscript indicates volume fraction (for instance, $\alpha^v = \alpha\rho/\rho_\alpha$).

A3. Bulk Magma Density

[86] Since volume fractions must sum to unity, $\alpha^v + c^v + \phi^v + \lambda^v = 1$, where α^v, c^v, ϕ^v, and λ^v are volume fractions of exsolved volatiles (bubbles), dissolved volatiles, phenocrysts, and melt. Converting to mass fractions using equation (A3), solving for ρ, and then substituting equations (A2a) and (A2b) yields

$$\rho = \left[\lambda\left(\frac{\chi_e}{\rho_\alpha} + \frac{\chi_d}{\rho_c} + \frac{1}{\rho_\lambda}\right) + \frac{\phi}{\rho_\phi}\right]^{-1}, \tag{A4}$$

where

$$\lambda = \frac{(1-\phi)}{(1+\chi_e+\chi_d)} \approx 1 - \phi, \tag{A5}$$

obtained by replacing α and c terms in $\alpha + c + \phi + \lambda = 1$ using equations (A2a) and (A2b) and then solving for λ. Note that λ is constant in the absence of crystallization or gas loss.

A4. Rate-and-State Friction

[87] The most common constitutive law for rate- and state-dependent friction gives the frictional resistance τ as [*Dieterich*, 1979; *Ruina*, 1983]

$$\tau = \overline{\sigma}\left[f_0 + a\ln\frac{v}{v_r} + b\ln\frac{\theta}{\theta_0}\right], \tag{A6}$$

where $\overline{\sigma}$ is the effective normal stress on the sliding surface, f_0 is the coefficient of friction at the reference sliding velocity v_r and reference state θ_0, v is sliding velocity, and a and b are dimensionless constants governing the direct and evolution effects. The state variable θ may be interpreted as the average time of contact between asperities on the sliding surfaces, and its evolution may be modeled using [*Dieterich*, 1979]

$$\frac{d\theta}{dt} = 1 - \frac{\theta v}{d_c}. \tag{A7}$$

[88] The reference state θ_0 is conventionally set to $\theta_0 = d_c/v_r$. Under sustained sliding at constant rate, lab experiments show that friction evolves to a steady state dependent on the instantaneous slip speed v [e.g., *Marone*, 1998]; that is, $d\theta/dt = 0$, and $\theta = d_c/v$. Substituting these expressions into equation (A6) yields

$$\tau = \overline{\sigma}\left[f_0 + (a-b)\ln\frac{v}{v_r}\right]. \tag{A8}$$

If a-b is positive, the fault is steady state strengthening (friction increases with an increase in sliding velocity), and if a-b is negative then it is rate weakening. Because a is always positive, if there is no state evolution and $b = 0$ (as is indicated by some high temperature experiments [*Blanpied et al.*, 1998]), then friction is necessarily velocity strengthening:

$$\tau = \overline{\sigma}\left[f_0 + a\ln\frac{v}{v_r}\right]. \tag{A9}$$

Rice et al. [2001] derived a regularized expression for rate-and-state friction which is suitable for zero velocity; with the steady state assumptions given above and $b = 0$, this specializes to equation (11).

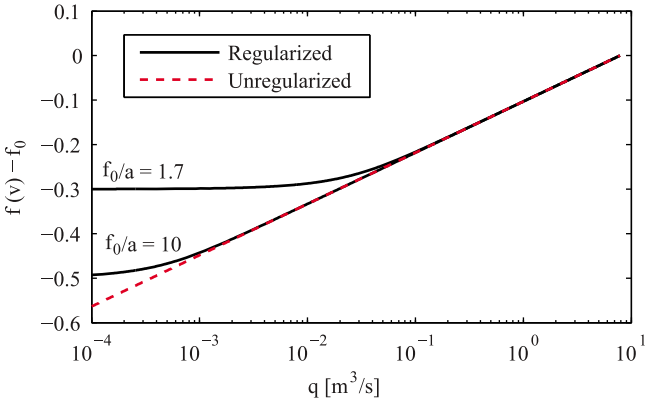

Figure A1. Regularized versus unregularized rate-dependent friction as a function of volume flux (assuming $R = 50$ m), for two different values of f_0/a, with $a = .05$ and $f_0 = [0.5, 0.2]$. Y axis shows effective coefficient of sliding friction $f(v) = \tau/\sigma$, minus f_0, such that the unregularized friction plots as $a\ln(v/v_r)$. Regularized friction approaches $f(v) = 0$ for small v, while unregularized does not. The effect of the regularization is more significant for smaller f_0/a.

A5. Analytical Models

[89] Solving the momentum balance (equation (1)) for v, converting to q using $v = q/\pi R^2$, approximating the pressure gradient dp/dz as a constant $-(p_{ch} - p_p)/L_c$, and combining with the expression for chamber pressure evolution (equation (13)) with no recharge yields

$$\frac{dp_{ch}}{dt} = \frac{\pi R^4}{8\overline{\eta}V_0(\beta_m + \beta_{ch})}\left(\frac{p_p - p_{ch}}{L_c} + \overline{\rho}g\right), \tag{A10}$$

where overbars on $\overline{\rho}$ and $\overline{\eta}$ indicate depth-averaged values.

[90] With no solid plug, surface pressure $p_p = 0$. Solving the resulting differential equation with initial condition $p(t = 0) = p_{ch_0}$, and assuming that β_m, $\overline{\rho}$ and $\overline{\eta}$ remain constant with time, yields the well-known exponential decay of chamber pressure with time

$$\Delta p_{ch}(t) = \Delta p_f\left(1 - e^{-t/t_c}\right), \tag{A11}$$

where Δp_{ch} is pressure change relative to the onset of the eruption, $\Delta p_f = \overline{\rho}gL_c - p_{ch_0}$, and time constant $t_c = 8\overline{\eta}V_0(\beta_m + \beta_{ch})\,L_c/\pi R^4$.

[91] Extruded volume V_{ex} may be calculated by integrating the flowrate with time [e.g., *Mastin et al.*, 2008]:

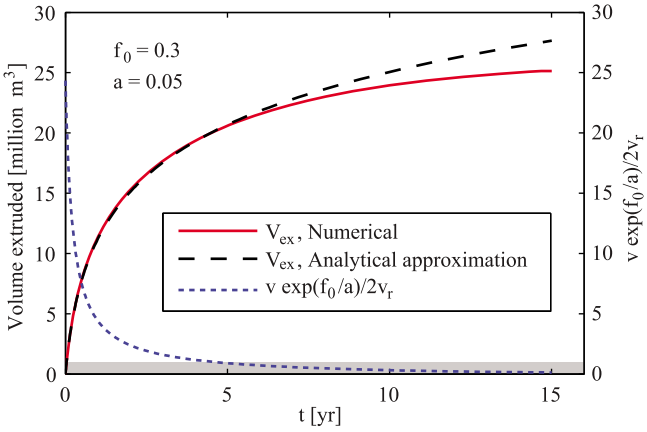

Figure A2. Numerical results with constant ρ and η in the conduit agree closely with the analytical approximation given in equation (A13), using $v_{t=0}$ from the numerical result. Agreement is better when $v\ \exp(f_0/a)/2v_r$ is large (gray shaded region at bottom indicates $v\ \exp(f_0/a)/2v_r < 1$). Differences become increasingly apparent late in the eruption when extrusion velocity is low. Note that 15 years are plotted to better show divergence.

$$\begin{aligned} V_{ex}(t) &= \int q dt = -V_0(\beta_m + \beta_{ch}) \int_0^t \frac{dp_{ch}}{dt'} dt' \\ &= -V_0(\beta_m + \beta_{ch}) \left[(p_{ch_0} - \overline{\rho} g L_c) e^{-t'/t_c} \right]_0^t \\ &= V_0(\beta_m + \beta_{ch})(p_{ch_0} - \overline{\rho} g L_c) \left(1 - e^{-t/t_c}\right) \\ &= -V_0(\beta_m + \beta_{ch}) \Delta p_{ch}, \end{aligned} \tag{A12}$$

where letting $t \to \infty$ yields a final extruded volume $V_f = -V_0(\overline{\beta}_m + \beta_{ch})\Delta p_f$. Extruded volume is therefore directly proportional to pressure change in the chamber, scaled by chamber volume and compressibility.

[92] *Mastin et al.* [2008] developed an expression for $V_{ex}(t)$ analogous to equation (A12) for a model which includes a solid plug slipping with unregularized rate-dependent friction (equation (A9)):

$$V_{ex}(t) = D \ln\left(1 + \frac{\pi R^2 v_{t=0}}{D} t\right), \tag{A13}$$

where $D = 2a\overline{\sigma} L V_0\ (\overline{\beta}_m + \beta_{ch})/R$ and $v_{t=0}$ is the extrusion velocity at the onset of the eruption.

[93] Because equation (A13) assumes unregularized rate-dependent friction it becomes unphysical for small velocities near the end of an eruption and it cannot be used to directly estimate either final values or time constant t_c. The expression also requires knowledge of velocity at $t = 0$, and this must be taken directly from observations or estimated through some other means.

[94] Equation (A13) does provide a useful means for verifying our model. To do so, we simplify the numerical calculation by using a constant η, a near-constant ρ (achieved by setting dissolved water content to zero), and plug density equal to the magma density. For $v_{t=0}$ in equation (A13) we use the initial velocity from the solution of the numerical model. The regularized friction law reduces to the log form when $(v/2v_r)\ \exp(f_0/a) \gg 1$ (Figure A1); we set $f_0 = 0.3$ and $a = .05$ and $v_r \approx v(t = 0)$. The ratio v/v_r is thus always less than 1, and is greatest at the onset of the eruption; we thus expect any divergence between numerical and analytical results to increase with time as $v \to 0$, as seen in Figure A2. Results agree closely for early in the eruption, providing validation of our numerical approach under these restricted conditions.

[95] **Acknowledgments.** The authors would like to thank Andrew Bradley for assistance with numerical techniques, Mike Lisowski for providing GPS time series, Larry Mastin for many valuable discussions, Jake Lowenstern for assistance with volatile solubility, and many at the Cascades Volcano Observatory for providing useful data, comments, and insights. Valuable reviews were provided by Oleg Melnik and one anonymous reviewer. This work was supported by NSF grant EAR-0537920.

References

Amoruso, A., and L. Crescentini (2009), Shape and volume change of pressurized ellipsoidal cavities from deformation and seismic data, *J. Geophys. Res.*, *114*, B02210, doi:10.1029/2008JB005946.

Barmin, A., O. Melnik, and R. S. J. Sparks (2002), Periodic behavior in lava dome eruptions, *Earth Planet. Sci. Lett.*, *199*, 173–184, doi:10.1016/S0012-821X(02)00557-5.

Barmin, A. A., O. Melnik, and A. Starostin (2003), Simulation of the effect of water injection on volcanic conduit flow, *Fluid Dyn.*, *38*(5), 95–105, doi:10.1023/B:FLUI.0000007836.27438.3b.

Blanpied, M. L., C. J. Marone, D. A. Lockner, J. D. Byerlee, and D. P. King (1998), Quantitative measure of the variation in fault rheology due to fluid-rock interactions, *J. Geophys. Res.*, *103*, 9691–9712, doi:10.1029/98JB00162.

Bonaccorso, A., and P. M. Davis (1999), Models of ground deformation from vertical volcanic conduits with application to eruptions of Mount St. Helens and Mount Etna, *J. Geophys. Res.*, *104*, 10,531–10,542, doi:10.1029/1999JB900054.

Cashman, K., and J. Blundy (2000), Degassing and crystallization of ascending andesite and dacite, *Philos. Trans. R. Soc. London A*, *358*(1770), 1487–1513, doi:10.1098/rsta.2000.0600.

Cashman, K. V., C. R. Thornber, and J. S. Pallister (2008), From dome to dust: Shallow crystallization and fragmentation of conduit magma during the 2004–2006 dome extrusion of Mount St. Helens, Washington, in *A Volcano Rekindled: The Renewed Eruption of Mount St. Helens, 2004–2006*, *U.S. Geol. Surv. Prof. Pap.*, *1750*, 387–413.

Collier, L., and J. Neuberg (2006), Incorporating seismic observations into 2D conduit flow modeling, *J. Volcanol. Geotherm. Res.*, *152*, 331–346, doi:10.1016/j.jvolgeores.2005.11.009.

Collombet, M. (2009), Two-dimensional gas loss for silicic magma flows: Toward more realistic numerical models, *Geophys. J. Int.*, *177*(1), 309–318, doi:10.1111/j.1365-246X.2008.04086.x.

Costa, A. (2005), Viscosity of high crystal content melts: Dependence on solid fraction, *Geophys. Res. Lett.*, *32*, L22308, doi:10.1029/2005GL024303.

Costa, A., O. Melnik, R. Sparks, and B. Voight (2007a), Control of magma flow in dykes on cyclic lava dome extrusion, *Geophys. Res. Lett.*, *34*, L02303, doi:10.1029/2006GL027466.

Costa, A., O. Melnik, and R. Sparks (2007b), Controls of conduit geometry and wallrock elasticity on lava dome eruptions, *Earth Planet. Sci. Lett.*, *260*, 137–15, doi:10.1016/j.epsl.2007.05.024.

Costa, A., R. Sparks, G. Macedonio, and O. Melnik (2009), Effects of wall-rock elasticity on magma flow in dykes during explosive eruptions, *Earth Planet. Sci. Lett.*, *288*, 455–462, doi:10.1016/j.epsl.2009.10.006.

de' Michieli Vitturia, M., A. Clarke, A. Neri, and B. Voight (2008), Effects of conduit geometry on magma ascent dynamics in dome-forming eruptions, *Earth Planet. Sci. Lett.*, *272*, 567–578, doi:10.1016/j.epsl.2008.05.025.

Dieterich, J. H. (1972), Time-dependent friction in rocks, *J. Geophys. Res.*, *77*, 3690–3697.

Dieterich, J. (1979), Modeling of rock friction: 1. Experimental results and constitutive equations, *J. Geophys. Res.*, *97*, 1859–1870.

Diller, K., A. B. Clarke, B. Voight, and A. Neri (2006), Mechanisms of conduit plug formation: Implications for vulcanian explosions, *Geophys. Res. Lett.*, *33*, L20302, doi:10.1029/2006GL027391.

Dzurisin, D. (2007), *Volcano Deformation: Geodetic Monitoring Techniques*, 476 pp., Springer, New York.

Eichelberger, J. (1995), Silicic volcanism: Ascent of viscous magmas from crustal reservoirs, *Annu. Rev. Earth Planet. Sci.*, *23*, 41–63.

Gerlach, T. M., K. A. McGee, and M. P. Doukas (2008), Emission rates of CO2, SO2, and H2S, scrubbing, and preeruption excess volatiles at Mount St. Helens, 2004–2005, in *A Volcano Rekindled: The Renewed Eruption of Mount St. Helens, 2004–2006*, *U.S. Geol. Surv. Prof. Pap.*, *1750*, 543–571.

Hautmann, S., J. Gottsmann, R. J. Sparks, A. Costa, O. Melnik, and B. Voight (2009), Modelling ground deformation caused by oscillating overpressure in a dyke conduit at Soufriere Hills Volcano, Montserrat, *Tectonophysics*, *471*(1–2), 87–95, doi:10.1016/j.tecto.2008.10.021.

Hess, K. U., and D. B. Dingwell (1996), Viscosities of hydrous leucogranitic melts: A non-Arrhenian model, *Am. Mineral.*, *81*(9–10), 1297–1300.

Huppert, H., and A. Woods (2002), The role of volatiles in magma chamber dynamics, *Nature*, *420*, 493–495, doi:10.1038/nature01211.

Huppert, H. E., J. B. Shepherd, R. H. Sigurdsson, and S. J. Sparks (1982), On lava dome growth, with application to the 1979 lava extrusion of the Soufriere of St. Vincent, *J. Volcanol. Geotherm. Res.*, *14*, 199–222, doi:10.1016/0377-0273(82)90062-2.

Jaupart, C. (1996), Physical models of volcanic eruptions, *Chem. Geol.*, *128*(1–4), 217–227.

Jaupart, C., and S. Tait (1990), Dynamics of eruptive phenomena, in *Modern Methods of Igneous Petrology: Understanding Magmatic Processes*, chap. 8, pp. 213–238, Mineral. Soc. of Am., Chantilly, Va.

Klug, C., and K. V. Cashman (1996), Permeability development in vesiculating magmas: Implications for fragmentation, *Bull. Volcanol.*, *58*(2), 87–100, doi:10.1007/s004450050128.

Lensky, N. G., R. S. J. Sparks, O. Navon, and V. Lyakhovsky (2008), Cyclic activity at Soufriere Hills Volcano, Montserrat: Degassing-induced pressurization and stick-slip extrusion, *Geol. Soc. Spec. Publ.*, *307*, 169–188.

Lin, W., and F. Heuze (1987), Comparison of in situ dynamic moduli and laboratory moduli of Mesaverde rocks, *Int. J. Rock Mech. Min. Sci. Geomech. Abstr.*, *24*(4), 257–263, doi:10.1016/0148-9062(87)90180-X.

Lisowski, M., D. Dzurisin, R. P. Denlinger, and E. Y. Iwatsubo (2008), Analysis of GPS-measured deformation associated with the 2004–2006 dome-building eruption of Mount St. Helens, Washington, in *A Volcano Rekindled: The Renewed Eruption of Mount St. Helens, 2004–2006*, *U.S. Geol. Surv. Prof. Pap.*, *1750*, 301–333.

Liu, Y., Y. Zhang, and H. Behrens (2005), Solubility of H2O in rhyolitic melts at low pressures and a new empirical model for mixed H2O-CO2 solubility in rhyolitic melts, *J. Volcanol. Geotherm. Res.*, *143*, 219–235, doi:10.1016/j.jvolgeores.2004.09.019.

Llewellin, E. W., and A. Manga (2005), Bubble suspension rheology and implications for conduit flow, *J. Volcanol. Geotherm. Res.*, *143*, 205–217.

Maeda, I. (2000), Nonlinear visco-elastic volcanic model and its application to the recent eruption of Mt. Unzen, *J. Volcanol. Geotherm. Res.*, *95*, 35–47, doi:10.1016/S0377-0273(99)00120-1.

Marone, C. (1998), Laboratory-derived friction laws and their application to seismic faulting, *Annu. Rev. Earth Planet. Sci.*, *26*, 643–696.

Mason, R., A. Starostin, O. Melnik, and R. Sparks (2006), From vulcanian explosions to sustained explosive eruptions: The role of diffusive mass transfer in conduit flow dynamics, *J. Volcanol. Geotherm. Res.*, *153*, 148–165, doi:10.1016/j.jvolgeores.2005.08.011.

Massol, H., C. Jaupart, and D. W. Pepper (2001), Ascent and decompression of viscous vesicular magma in a volcanic conduit, *J. Geophys. Res.*, *106*, 16,223–16,240.

Mastin, L. G. (2005), The controlling effect of viscous dissipation on magma flow in silicic conduits, *J. Volcanol. Geotherm. Res.*, *143*, 17–28.

Mastin, L. G., and M. S. Ghiorso (2000), A numerical program for steady-state flow of magma-gas mixtures through vertical eruptive conduits, 56 pp., *U.S. Geol. Surv. Open File Rep., 00-209*.

Mastin, L. G., E. Roeloffs, N. M. Beeler, and J. E. Quick (2008), Constraints on the size, overpressure, and volatile content of the Mount St. Helens magma system from geodetic and dome-growth measurements during the 2004–2006+ eruption, in *A Volcano Rekindled: The Renewed Eruption of Mount St. Helens, 2004–2006*, *U.S. Geol. Surv. Prof. Pap.*, *1750*, 461–488.

Mastin, L. G., M. Lisowski, E. Roeloffs, and N. Beeler (2009), Improved constraints on the estimated size and volatile content of the Mount St. Helens magma system from the 2004–2008 history of dome growth and deformation, *Geophys. Res. Lett.*, *36*, L20304, doi:10.1029/2009GL039863.

McTigue, D. F. (1987), Elastic stress and deformation near a finite spherical magma body: Resolution of the point source paradox, *J. Geophys. Res.*, *92*, 12,931–12,940.

Melnik, O., and R. S. J. Sparks (1999), Nonlinear dynamics of lava dome extrusion, *Nature*, *402*, 37–41, doi:10.1038/46950.

Melnik, O. E., and R. S. J. Sparks (2002), Dynamics of magma ascent and extrusion at Soufriere Hills Volcano, Montserrat, in *The Eruption of Soufriere Hills Volcano, Montserrat, from 1995 to 1999*, *Mem. Geol. Soc. London*, *21*, 153–171, doi:10.1144/GSL.MEM.2002.021.01.07.

Melnik, O., and R. S. J. Sparks (2005), Controls on conduit magma flow dynamics during lava dome building eruptions, *J. Geophys. Res.*, *110*, B02209, doi:10.1029/2004JB003183.

Melnik, O., and S. Sparks (2006), Transient models of conduit flows during volcanic eruptions, in *Statistics in Volcanology*, pp. 201–214, Geol. Soc., London.

Mogi, K. (1958), Relations between the eruptions of various volcanoes and the deformations of the ground surfaces around them, *Bull. Earthquake Res. Inst. Univ. Tokyo*, *36*, 99–134.

Nakada, S., H. Shimizu, and K. Ohta (1999), Overview of the 1990–1995 eruption at Unzen Volcano, *J. Volcanol. Geotherm. Res.*, *89*, 1–22, doi:10.1016/S0377-0273(98)00118-8.

Newman, S., and J. B. Lowenstern (2002), VolatileCalc: A silicate melt-H2O-CO2 solution model written in Visual Basic for Excel, *Comput. Geosci.*, *28*(5), 597–604, doi:10.1016/S0098-3004(01)00081-4.

Nishimura, T. (2006), Ground deformation due to magma ascent with and without degassing, *Geophys. Res. Lett.*, *33*, L23309, doi:10.1029/2006GL028101.

Nishimura, T. (2009), Ground deformation caused by magma ascent in an open conduit, *J. Volcanol. Geotherm. Res.*, *187*, 178–192, doi:10.1016/j.jvolgeores.2009.09.001.

Ochs, F. A., and R. A. Lange (1999), The density of hydrous magmatic liquids, *Science*, *283*(5406), 1314–1317, doi:10.1126/science.283.5406.1314.

Owen, S., P. Segall, M. Lisowski, A. Miklius, M. Murray, M. Bevis, and J. Foster (2000), January 30, 1997 eruptive event on Kilauea Volcano, Hawaii, as monitored by continuous GPS, *Geophys. Res. Lett.*, *27*, 2757–2760, doi:10.1029/1999GL008454.

Proussevitch, A., and D. Sahagian (2005), Bubbledrive-1: A numerical model of volcanic eruption mechanisms driven by disequilibrium magma degassing, *J. Volcanol. Geotherm. Res.*, *143*, 89–111, doi:10.1016/j.jvolgeores.2004.09.012.

Ramos, J. I. (1995), One-dimensional, time-dependent, homogeneous, two-phase flow in volcanic conduits, *I. J. Numer. Methods Fluids*, *21*(3), 253–278, doi:10.1002/fld.1650210306.

Rice, J. R., N. Lapusta, and K. Ranjith (2001), Rate and state dependent friction and the stability of sliding between elastically deformable solids, *J. Mech. Phys. Solids*, *49*, 1865–1898.

Rivalta, E., and P. Segall (2008), Magma compressibility and the missing source for some dike intrusions, *Geophys. Res. Lett.*, *35*, L04306, doi:10.1029/2007GL032521.

Ruina, A. (1983), Slip instability and state variable friction laws, *J. Geophys. Res.*, *88*, 10,359–10,370.

Schilling, S. P., R. A. Thompson, J. A. Messerich, and E. Y. Iwatsubo (2008), Use of digital aerophotogrammetry to determine rates of lava dome growth, Mount St. Helens, 2004–2005, *A Volcano Rekindled: The Renewed Eruption of Mount St. Helens, 2004–2006*, *U.S. Geol. Surv. Prof. Pap.*, *1750*, 145–167.

Segall, P. (2010), *Earthquake and Volcano Deformation*, 432 pp., Princeton Univ. Press, Princeton, N. J.

Segall, P., P. Cervelli, S. Owen, M. Lisowski, and A. Miklius (2001), Constraints on dike propagation from continuous GPS measurements, *J. Geophys. Res.*, *106*, 19,301–19,317.

Slezin, Y. B. (2003), The mechanism of volcanic eruptions (a steady state approach), *J. Volcanol. Geotherm. Res.*, *122*, 7–50, doi:10.1016/S0377-0273(02)00464-X.

Sparks, R. S. J. (1997), Causes and consequences of pressurisation in lava dome eruptions, *Earth Planet. Sci. Lett.*, *150*, 177–189.

Starostin, A., A. Barmin, and O. Melnik (2005), A transient model for explosive and phreatomagmatic eruptions, *J. Volcanol. Geotherm. Res.*, *143*, 133–151, doi:10.1016/j.jvolgeores.2004.09.014.

Stasiuk, M. V., C. Jaupart, and R. S. J. Sparks (1993), On the variations of flow-rate in nonexplosive lava eruptions, *Earth Planet. Sci. Lett.*, *114*, 505–516, doi:10.1016/0012-821X(93)90079-O.

Takeuchi, S., S. Nakashima, A. Tomiya, and H. Shinohara (2005), Experimental constraints on the low gas permeability of vesicular magma during decompression, *Geophys. Res. Lett.*, *32*, L10312, doi:10.1029/2005GL022491.

Timoshenko, S., and J. Goodier (1970), *Theory of Elasticity*, McGraw-Hill, New York.

Wadge, G. (1981), The variations of magma discharge during basaltic eruptions, *J. Volcanol. Geotherm. Res.*, *11*, 139–168, doi:10.1016/0377-0273(81)90020-2.

Woods, A., and H. Huppert (2003), On magma chamber evolution during slow effusive eruptions, *J. Geophys. Res.*, *108*(B8), 2403, doi:10.1029/2002JB002019.

Woods, A. W., and T. Koyaguchi (1994), Transitions between explosive and effusive eruptions of silicic magmas, *Nature*, *370*, 641–644, doi:10.1038/370641a0.

Wright, T. J., C. Ebinger, J. Biggs, A. Ayele, G. Yirgu, D. Keir, and A. Stork (2006), Magma-maintained rift segmentation at continental rupture in the 2005 Afar dyking episode, *Nature*, *442*, 291–294, doi:10.1038/nature04978.

Yang, X. M., P. M. Davis, and J. H. Dieterich (1988), Deformation from inflation of a dipping finite prolate spheroid in an elastic half-space as a model for volcanic stressing, *J. Geophys. Res.*, *93*, 4249–4257.

K. Anderson and P. Segall, Department of Geophysics, Stanford University, Stanford, CA 94305, USA. (kander@stanford.edu)